First-principles characterization of thermal conductivity in LaPO$_4$-based alloys

Anees Pazhedath[1], Lorenzo Bastonero[1], Nicola Marzari[1,2,3] and Michele Simoncelli[4,*]

[1]*U Bremen Excellence Chair, Bremen Center for Computational Materials Science, and MAPEX Center for Materials and Processes, University of Bremen, Bremen D-28359, Germany*

[2]*Theory and Simulation of Materials (THEOS) and National Centre for Computational Design and Discovery of Novel Materials (MARVEL), École Polytechnique Fédérale de Lausanne, Switzerland*

[3]*Laboratory for Materials Simulations, Paul Scherrer Institute, Villigen PSI 5232, Switzerland*

[4]*Cavendish Laboratory, Theory of Condensed Matter Group, University of Cambridge, United Kingdom*

Alloys based on lanthanum phosphate (LaPO$_4$) are often employed as thermal barrier coatings, due to their low thermal conductivity and structural stability over a wide temperature range. To enhance the thermal-insulation performance of these alloys, it is essential to comprehensively understand the fundamental physics governing their heat conduction. Here, we employ the Wigner formulation of thermal transport in conjunction with first-principles calculations to elucidate how the interplay between anharmonicity and compositional disorder determines the thermal properties of La$_{1-x}$Gd$_x$PO$_4$ alloys, and discuss the fundamental physics underlying the emergence and coexistence of particlelike and wavelike heat-transport mechanisms. We also show how the Wigner transport equation correctly describes the thermodynamic limit of a compositionally disordered crystal, while the Boltzmann transport equation does not. Our predictions for microscopic vibrational properties (temperature-dependent Raman spectrum) and for macroscopic thermal conductivity are validated against experiments. Finally, we leverage these findings to devise strategies to optimize the performance of thermal barrier coatings.

I. INTRODUCTION

Improving the thrust and efficiency of airbreathing jet engines requires increasing the temperature of the gas at the entry of their turbine cascade (inlet temperature) [1]. Since the 1970s, significant research efforts have been made to develop materials capable of operating at increasingly higher temperatures, and current turbines employ superalloy blades covered by thermal barrier coatings (TBCs) [2–5]. TBCs are critical in determining the performance and lifespan of turbines: they protect the blades from thermal stresses, allowing operational temperatures higher than the melting point of the superalloy. Thus, one of the key objectives [6–8] in current research on TBCs is to find materials with the lowest possible thermal conductivity [1,2].

Hitherto, most of the progress on improving the thermal-insulation performance of TBC materials has relied on experiments and trial-and-error efforts, which hinted that the presence of compositional disorder in highly anharmonic materials can be beneficial for their thermal-insulation performance [9,10]. However, a first-principles understanding of the microscopic physics governing heat conduction in these materials is missing, preventing their systematic optimization. The absence of such understanding on how the interplay between anharmonicity and compositional disorder affects the transport properties of the TBC can be traced back to limitations of established first-principles approaches for thermal transport in solids, namely, first-principles molecular dynamics (FPMD) [11–16] and the linearized Boltzmann transport equation (LBTE) for phonons [17–25]. Specifically, despite recent advances [26,27], FPMD approaches still have a high computational cost, which practically limits their application to materials having nanometric disorder length scale (simulation cells containing a few hundred atoms). On the other hand, the LBTE accounts exclusively for particlelike (intraband) heat transport mechanisms and misses wavelike interband tunneling; thus, it is in principle accurate only in weakly anharmonic crystals characterized by well-separated phonon bands [28]. The LBTE with a perturbative description of compositional (mass) disorder [29] has been shown to successfully describe the thermal

properties of SiGe alloys [30], i.e., weakly anharmonic materials in which low-frequency vibrational modes dominate transport [31]. However, such a perturbative scheme fails in strongly anharmonic systems where transport is not dominated by low-frequency modes [32]. Thermal insulators and alloys for TBCs [33,34] belong to this class; thus, the effect of compositional disorder on the thermal conductivity of these materials cannot be described using the perturbative treatment within the LBTE.

These limitations can be overcome by relying on the recently introduced Wigner transport equation (WTE) [28]. Specifically, the WTE generalizes the LBTE by accounting not only for the particlelike propagation of populations of phonons, but also for wavelike tunneling between vibrational eigenstates with an energy difference smaller than their linewidths. The former transport mechanism is commonly called "intraband," or "band-diagonal" transport; the latter is often referred to as "interband" transport, originating from the band-off-diagonal elements of the Wigner density matrix, also known as "coherences" [33]. Accounting for both these transport mechanisms allows one to unify under the same formal equation the LBTE for weakly anharmonic crystals and the Allen-Feldman equation for disordered solids [35], also covering all the intermediate cases—such as alloys for TBC materials—in which anharmonicity [33,36–40] and disorder [41–45] are both relevant.

Here, we combine first-principles calculations with the Wigner formulation to unveil the microscopic heat conduction mechanisms in LaPO$_4$ [7,46–49], in its solid solutions with GdPO$_4$, and its composites with La$_2$Zr$_2$O$_7$. These materials are employed in TBCs [7,46–49] due to their low thermal conductivity [46–49], high melting point [50], chemical durability [51], structural stability [52], and large thermal expansion coefficient [53] over a wide temperature range. After characterizing the properties of the heat carriers in LaPO$_4$, we show that microscopic particlelike and wavelike transport mechanisms emerge and coexist in this material, and we discuss how they contribute to the macroscopic thermal conductivity. Next, we analyze how atomic scale compositional disorder affects thermal transport in La$_{1-x}$Gd$_x$PO$_4$ alloys, describing La-Gd mass-substitutional disorder explicitly using models containing up to 5184 atoms. Finally, we use the continuum Maxwell model for the effective conductivity of composites [54,55] to discuss how thermal conductivity is affected by compositional disorder at the micrometer scale, investigating composites containing micrometer-sized grains of La$_2$Zr$_2$O$_7$ and LaPO$_4$ at different concentrations.

II. WIGNER FORMULATION FOR THERMAL TRANSPORT

The WTE [28,33] describes thermal transport in solids accounting for the interplay between structural disorder, anharmonicity, and Bose-Einstein statistics of vibrations. Such an equation provides a comprehensive approach to thermal transport in solids, allowing one to describe structurally ordered "simple crystals" with interband spacings much larger than the linewidths [56,57], glasses [43–45], as well as the intermediate regime of "complex crystals" with interband spacings smaller than the linewidths [33,36–38]. In the following, we summarize the salient features of the WTE. For complex crystals having ultralow thermal conductivity, the WTE can be accurately solved using the single-mode relaxation-time approximation (SMRTA) [30,44,58], since in these cases the SMRTA yields results practically indistinguishable from the exact solution [28,33,37,38,44]. Within the SMRTA, the Wigner conductivity expression assumes the compact form

$$\kappa_T^{\alpha\beta} = \frac{1}{\mathcal{V}N_c} \sum_{\mathbf{q},s,s'} \frac{\omega(\mathbf{q})_s + \omega(\mathbf{q})_{s'}}{4} \left(\frac{C(\mathbf{q})_s}{\omega(\mathbf{q})_s} + \frac{C(\mathbf{q})_{s'}}{\omega(\mathbf{q})_{s'}} \right) v^\alpha(\mathbf{q})_{s,s'} v^\beta(\mathbf{q})_{s',s} \frac{[\Gamma(\mathbf{q})_s + \Gamma(\mathbf{q})_{s'}]/2}{[\omega(\mathbf{q})_s - \omega(\mathbf{q})_{s'}]^2 + [\Gamma(\mathbf{q})_s + \Gamma(\mathbf{q})_{s'}]^2/4}, \quad (1)$$

where $\hbar\omega(\mathbf{q})_s$ is the energy of the phonon having wave vector $\mathbf{q}$ and mode index s, which carries the specific heat

$$C(\mathbf{q})_s = C[\omega(\mathbf{q})_s] = \frac{\hbar^2\omega^2(\mathbf{q})_s}{k_B T^2} \bar{N}(\mathbf{q})_s[\bar{N}(\mathbf{q})_s + 1], \quad (2)$$

where $\bar{N}(\mathbf{q})_s = \{\exp[\hbar\omega(\mathbf{q})_s/k_B T] - 1\}^{-1}$ is the Bose-Einstein distribution at temperature T, $v^\alpha(\mathbf{q})_{s,s'}$ is the velocity operator coupling eigenstates s and s' at the same wave vector $\mathbf{q}$ (α denotes a Cartesian direction) [33], N_c is the number of $\mathbf{q}$ points entering in the $\mathbf{q}$ summation, and $\mathcal{V}$

is the primitive-cell volume; finally, $\hbar\Gamma(\mathbf{q})_s = \hbar\Gamma(\mathbf{q})_s^{\text{anh}} + \hbar\Gamma(\mathbf{q})_s^{\text{imp}} + \hbar\Gamma(\mathbf{q})_s^{\text{bnd}}$ is the total linewidth, determined by anharmonicity [18,59] [$\hbar\Gamma(\mathbf{q})_s^{\text{anh}}$], isotopic impurity disorder [29] [$\hbar\Gamma(\mathbf{q})_s^{\text{imp}}$], and grain-boundary scattering [60,61] [$\hbar\Gamma(\mathbf{q})_s^{\text{bnd}}$]; see Appendix A for details. We stress that the damping (linewidths) of phonons due to the presence of isotopes is taken into account perturbatively using the approach introduced by Tamura [29]. This model predicts the isotopic impurity linewidth to be proportional to the variance of the distribution of the isotopic masses [see Eq. (A3) in Appendix A]; we also note that, for the

elements considered here (La, Gd, P, O), this variance yields isotopic impurity linewidths negligible compared to anharmonic linewidths (see Appendix E for details). In contrast, the large mass disorder due to La→Gd substitution in $La_{1-x}Gd_xPO_4$ alloys will be taken into account exactly using the Wigner formulation (more on this later), since recent work [32] has shown that Tamura's perturbative treatment fails in systems where heat transport is not dominated by low-frequency (acoustic) vibrations.

In crystals, it is useful to resolve the WTE conductivity (1) as the sum of two terms, $\kappa_T = \kappa_P + \kappa_C$ [33]. The term κ_P is referred to as "populations conductivity" [28,33] and is determined by the diagonal ($s = s'$) or perfectly degenerate [$s \neq s'$ with $\omega(\mathbf{q})_s = \omega(\mathbf{q})_{s'}$] terms in the summation in (1). Specifically, κ_P can be written as $\kappa_P^{\alpha\beta} = 1/(\mathcal{V}N_c) \sum_{\mathbf{q},s} C[\omega(\mathbf{q})_s]v^\alpha(\mathbf{q})_{s,s}\Lambda^\beta(\mathbf{q})_s$; this expression shows that κ_P describes a heat-transport mechanism in which heat carriers transport the energy $\hbar\omega(\mathbf{q})_s$ and propagate particlelike with velocity $v^\alpha(\mathbf{q})_{s,s}$ over the mean free path $\Lambda^\beta(\mathbf{q})_s = v^\beta(\mathbf{q})_{s,s}[\Gamma(\mathbf{q})_s]^{-1}$, in analogy with particles in a classical gas. In contrast, the nondegenerate off-diagonal elements (referred to as "coherences" [28,33]) do not have an absolute energy, but are characterized by an energy difference $\hbar\omega(\mathbf{q})_s - \hbar\omega(\mathbf{q})_{s'}$; they describe conduction through a wavelike tunneling mechanism between pairs of phonon bands (a mechanism bearing analogies to the electronic Zener interband tunneling [62]). In Eq. (1), nondegenerate off-diagonal elements determine the coherences conductivity κ_C [28,33]. It has been shown in Refs. [28,33,63] that in simple crystals particlelike mechanisms dominate over the wavelike tunneling and thus $\kappa_P \gg \kappa_C$, while in complex crystals both these mechanisms coexist and may have comparable strength, implying that $\kappa_P \sim \kappa_C$. Finally, Refs. [44,45,64] have shown that in strongly disordered oxide glasses $\kappa_P \ll \kappa_C$.

III. RESULTS AND DISCUSSION

A. $LaPO_4$: vibrational properties and Raman spectra

In order to elucidate the microscopic physics that governs thermal transport in $LaPO_4$-based alloys, we start by computing from first principles the microscopic vibrational properties appearing in the thermal conductivity expression (1) for the fundamental component $LaPO_4$. Specifically, we employ density-functional theory (DFT) to optimize the geometry (see Fig. 14 in Appendix F), to compute the vibrational harmonic frequencies [65] (see Appendix F, in particular the phonon dispersions are shown in Fig. 15, and the phonon density of states is shown in Fig. 16) and anharmonic third-order linewidths [18,19,21] (see Fig. 10 in Appendix B). These quantities are calculated employing the standard perturbative approach, where frequencies and velocity operators are determined at the harmonic level and considered temperature independent, and the anharmonic linewidths depend

on temperature through the Bose-Einstein distribution [see Eq. (A1) in Appendix A]. In order to assess the accuracy of this perturbative approach in describing the actual frequencies and linewidths, we employ the theoretical frequencies and linewidths to predict the temperature dependence of the experimentally measurable nonresonant Raman spectra [68],

$$I(\omega, T) \propto \sum_s I_s(T) \frac{(\Gamma_s + \Gamma_{\text{ins}})/2}{(\omega - \omega_s)^2 + (\Gamma_s + \Gamma_{\text{ins}})^2/4}, \quad (3)$$

where $I_s(T)$ is the Raman intensity of the phonon mode s computed within the Placzek approximation and using the powder average formula [Eq. (5) in Ref. [69]], including the laser-frequency factor at experimental conditions; ω_s and Γ_s are the bare phonon frequencies and total linewidths at $\mathbf{q} = \mathbf{0}$. The linewidths are the full width at half maximum, related to the lifetime as $\tau_s = [\Gamma_s]^{-1}$, and are determined by both anharmonicity (Γ_s^{anh}) and isotopic impurity disorder (Γ_s^{imp}), i.e., $\Gamma_s = \Gamma_s^{\text{imp}} + \Gamma_s^{\text{anh}}$, respectively. Finally, $\Gamma_{\text{ins}} = 2\,\text{cm}^{-1}$ accounts for the instrumental broadening [70] affecting the experiments [66,67] with which we compare our calculations. In this approach the temperature dependence of the Raman spectra originates from the Bose-Einstein occupation numbers appearing in the intensity $I_s(T)$, and from the linewidths appearing in the Lorentzian broadening, as in previous work [33].

We show in Fig. 1 a comparison between the theoretical and experimental Raman intensities in powder samples at 300 K (experiments by Hirsh *et al.* [67]) and at 1000 K (experiments by Lucas *et al.* [66]). Then, we note that the theoretical and experimental spectra are systematically shifted by approximately 26 cm^{-1}. Systematic, rigid shifts between the theoretical and experimental spectra comparable to those observed here are common in the literature, and the small relative discrepancies ($\lesssim 2.5\%$ for the optical modes) observed here are within the accuracy with which DFT predictions usually describe experiments [71–73]. We also note that energy shifts in the symmetric or asymmetric PO_4 stretching modes around 1000 cm^{-1} may be related to the presence of water in the experimental samples [66,67,73], which is not accounted for in our calculations. More importantly, the positions of the experimental peaks are essentially unaffected by temperature; this indicates that in $LaPO_4$, the temperature renormalization of the vibrational frequencies, not accounted for in the standard perturbative treatment of anharmonicity employed here, is unimportant. In the insets of Fig. 1, we highlight how the broadening of the experimental Raman peaks—which is determined mainly by anharmonicity and is negligibly affected by compositional disorder [67]—is in agreement with our theoretical predictions at all temperatures for the most intense, high-frequency part of the Raman spectrum. We recall that the anharmonic linewidths generally increase with frequency and
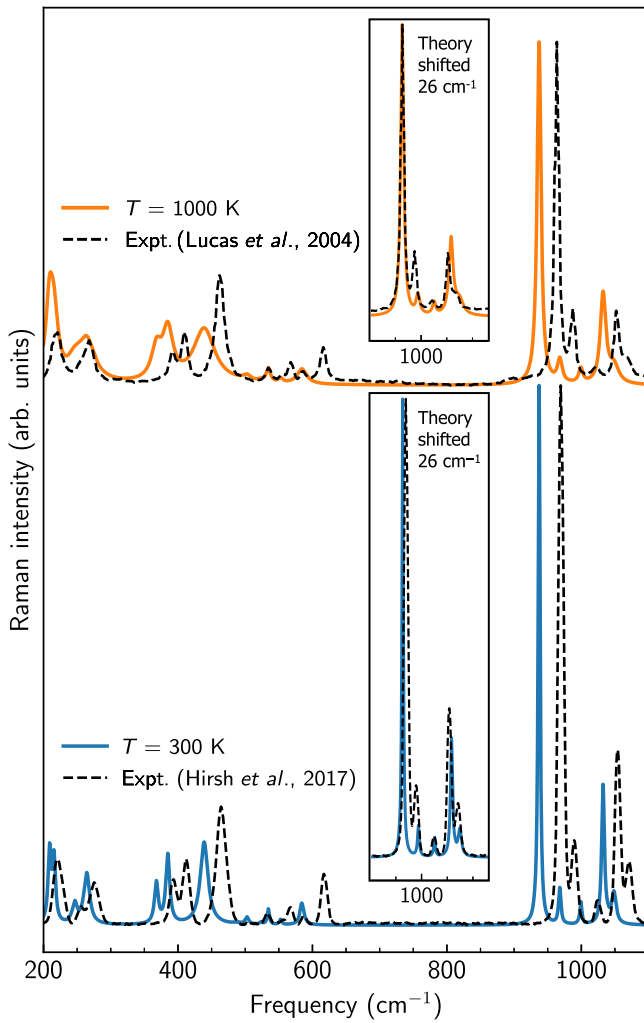
FIG. 1. Temperature-dependent Raman spectra. Solid lines are theory at 1000 K (top) and 300 K (bottom); dashed lines are experimental data, from Lucas *et al.* [66] at 1000 K (top) and from Hirsh *et al.* [67] at 300 K (bottom). In the insets, the theoretical spectra have been rigidly shifted by 26 cm^{-1} to higher frequencies (right) to ease the comparison between the broadening of the theoretical and experimental spectra.

temperature [33,36,44,45] (see Fig. 10 in Appendix B). Thus, from the good agreement between the theoretical and experimental broadening at high frequencies—where anharmonic effects are usually largest—we infer that the standard perturbative approach employed here provides a description of the anharmonic microscopic vibrational properties of LaPO$_4$ that is sufficiently accurate for our purposes. Finally, we note that the low-frequency part of the experimental Raman spectrum at 1000 K is sharper than the theoretical predictions. Such behavior may be due to the occurrence of grain coalescence in the sample of Lucas *et al.* [66], which could cause partial crystallization and departure from our calculations that assume a powder sample. Additional details on the Raman simulations are reported in Appendix F 2.

B. Thermal conductivity of LaPO$_4$

In this section, we use the first-principles microscopic vibrational properties of LaPO$_4$ to evaluate the thermal conductivity as a function of temperature [Eq. (1)]. Figure 2 shows our theoretical predictions for a bulk sample (i.e., without considering grain-boundary scattering; more on this later); these are compared with experiments by Hongying *et al.* [47], Aibing *et al.* [46], Chenglong *et al.* [48], and Shijina *et al.* [49]. Theory and experiments are in overall good agreement (more details on the spread of the experimental data will be discussed later), both approaching a T^{-1} trend at low temperature and a milder-than-T^{-1} decay at high temperature. These different trends in the low- and high-temperature limits emerge from the coexistence of particlelike and wavelike transport mechanisms, whose relative strength depends on temperature. Specifically, Fig. 2 shows that the particlelike mechanisms—which determine the populations conductivity κ_P discussed in Sec. II—dominate at low temperature. This is a consequence of the increase of $\kappa_P(T)$ upon lowering temperature T, which can be understood by recalling that the particlelike conductivity emerging from the Wigner formulation is totally equivalent to the LBTE conductivity [33], and in crystals characterized by dominant third-order anharmonicity, the latter universally follows a $\kappa_P(T) \sim T^{-1}$ scaling for $T > T_D$, where T_D is the Debye temperature [74–77]. For LaPO$_4$, $T_D \sim 144$ K [78], explaining why $\kappa_P(T) \propto T^{-1}$ for $T > 200$ K. In contrast,
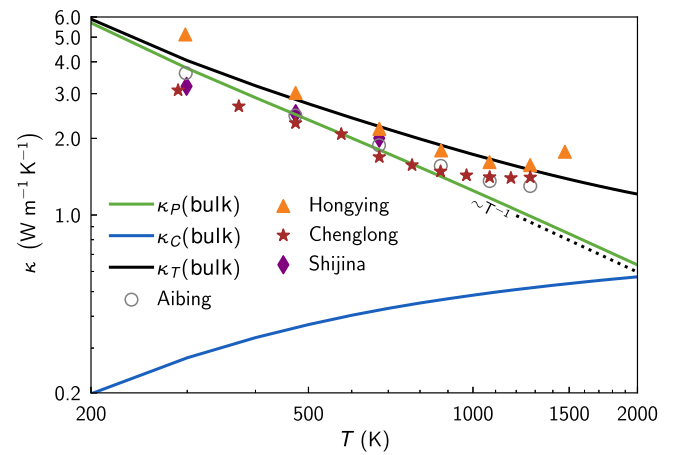

FIG. 2. Thermal conductivity of LaPO$_4$. Green line denotes the populations conductivity κ_P, which follows the T^{-1} decay typical of Peierls' particlelike transport in crystals with dominant third-order anharmonicity. Blue line denotes the coherences conductivity κ_C, significant at high temperature. Black line denotes the total conductivity, $\kappa_T = \kappa_P + \kappa_C$. Scatter points are experiments from Aibing *et al.* [46], Hongying *et al.* [47], Chenglong *et al.* [48], and Shijina *et al.* [49]. The theoretical conductivities are the average trace of the respective tensors; these are estimators for the conductivity of the polycrystalline samples employed in experiments [79].

wavelike mechanisms yield a coherences conductivity κ_C that in LaPO$_4$ increases with temperature and determines the milder-than-T^{-1} decay at high temperature.

Now we focus on the spread displayed by different, independent experiments [46–49], which is deemed to originate from differences in the samples. Specifically, the conductivity is sensitive to the sample's grain properties and size [47,80,81], which are determined by the synthesis process. The experiments that are closest to our bulk (perfect-crystal) calculations are those by Hongying *et al.* [47], who used heat treatment to obtain samples with a high degree of crystallinity (average grain size $\gtrsim 25$ μm). We also note that the highest-temperature experiment performed by Hongying *et al.* [47] ($T \sim 1500$ K) departs from the decreasing trend displayed by all the other experiments discussed in the same reference. This change in trend might originate from the onset of the radiative conduction; the description of this effect goes beyond the scope of the present study. The other experiments reported in Fig. 2 show a lower conductivity, which originates from the smaller average grain size and consequent stronger grain-boundary scattering in these samples. Specifically, the samples used by Shijina *et al.* [49] had grains with a size of 1–4 μm, Aibing *et al.* [46] used samples with grains in the 1–3 μm range, and Chenglong *et al.* [48] used samples with grains in the 2–5 μm range. We show in Fig. 3 that accounting for grain-boundary scattering at the micrometer length scale [see Eq. (A4) in Appendix A] produces variations of the total thermal conductivity that are broadly compatible with the spread observed in different

experiments. Finally, we note that Fig. 3 also reports predictions for samples with nanometer-sized grains (blue and red curves); this is to provide information on how much the conductivity would change if the experimental nanostructuring techniques for the TBC (see, e.g., Refs. [82,83]) were used to prepare the samples.

C. Particlelike and wavelike transport

The calculations in the previous section highlighted how the macroscopic thermal conductivity is determined by both particlelike and wavelike microscopic transport mechanisms. In this section, we investigate these microscopic transport mechanisms; specifically, how their relative strengths and contributions to the total macroscopic conductivity vary as a function of temperature. As discussed in Ref. [33], it is possible to resolve how much each phonon $(\mathbf{q})_s$ contributes to the particlelike [$\bar{\mathcal{K}}_P(\mathbf{q})_s$] and wavelike [$\bar{\mathcal{K}}_C(\mathbf{q})_s$] conductivities (the bar denotes the average trace of the mode-resolved contributions to the particlelike and wavelike conductivity tensors; full expressions are reported in Appendix C). Simoncelli *et al.* [33] demonstrated that the relative strength of these contributions scales as the ratio between the average interband spacings ($\Delta\omega_{\mathrm{avg}} = \omega_{\max}/3N_{\mathrm{at}}$, where $\omega_{\max}$ is the maximum phonon frequency, N_{at} is the number of atoms in the primitive cell, and $3N_{\mathrm{at}}$ is the number of phonon bands) and the linewidth $\Gamma(\mathbf{q})_s = [\tau(\mathbf{q})_s]^{-1}$ [here $\tau(\mathbf{q})_s$ is the phonon lifetime]:

$$\frac{\bar{\mathcal{K}}_C(\mathbf{q})_s}{\bar{\mathcal{K}}_P(\mathbf{q})_s} \simeq \frac{\Gamma(\mathbf{q})_s}{\Delta\omega_{\mathrm{avg}}} = \frac{[\Delta\omega_{\mathrm{avg}}]^{-1}}{\tau(\mathbf{q})_s}. \tag{4}$$

Equation (4) predicts that phonons having a lifetime $\tau(\mathbf{q})_s$ equal to the inverse interband spacing $[\Delta\omega_{\mathrm{avg}}]^{-1}$ (also referred to as the "Wigner limit in time" [33]) contribute simultaneously and with equal strength to both particlelike and wavelike conduction mechanisms. In contrast, phonons with a lifetime much longer (shorter) than the Wigner limit in time contribute predominantly to the particlelike (wavelike) conductivity. Finally, Eq. (4) predicts the transition between these two limits to be nonsharp and centered at the Wigner limit in time. These analytical expectations are verified numerically in Fig. 4. Specifically, in the upper panel of the figure, we show the distribution of phonon lifetimes as a function of phonon energies at different temperatures. For each phonon mode (individual scatter point in Fig. 4), we use the particlelike and wavelike conductivity contributions [$\bar{\mathcal{K}}_P(\mathbf{q})_s$ and $\bar{\mathcal{K}}_C(\mathbf{q})_s$ appearing in Eq. (4), respectively] to resolve the conduction mechanisms through which the phonon participates to heat transport, as well as how much the microscopic phonon mode contributes to the macroscopic conductivity. The first piece of information on the type of conduction mechanism is encoded in the color of the scatter point,
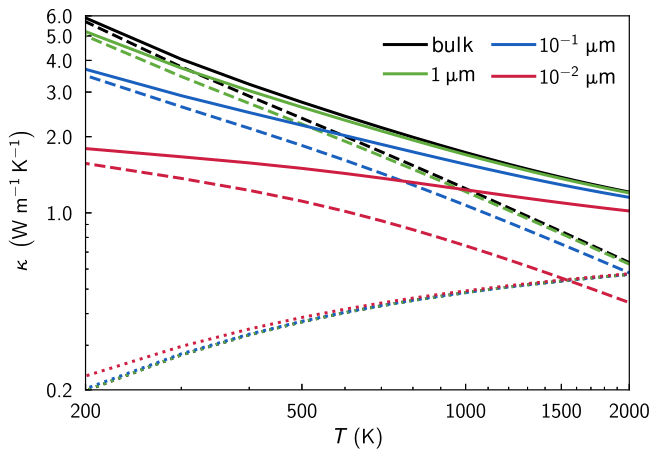

FIG. 3. Effect of grain-boundary scattering on the conductivity. We considered grain sizes equal to 10^{-2} (red), 10^{-1} (blue), and 1 μm (green) to compute the conductivity, and we compared results with the bulk value (black). The solid, dashed, and dotted lines are κ_T, κ_P, and κ_C, respectively. Each line is the average trace of the respective conductivity tensor, an estimator for the conductivity of the polycrystalline samples employed in experiments [79].
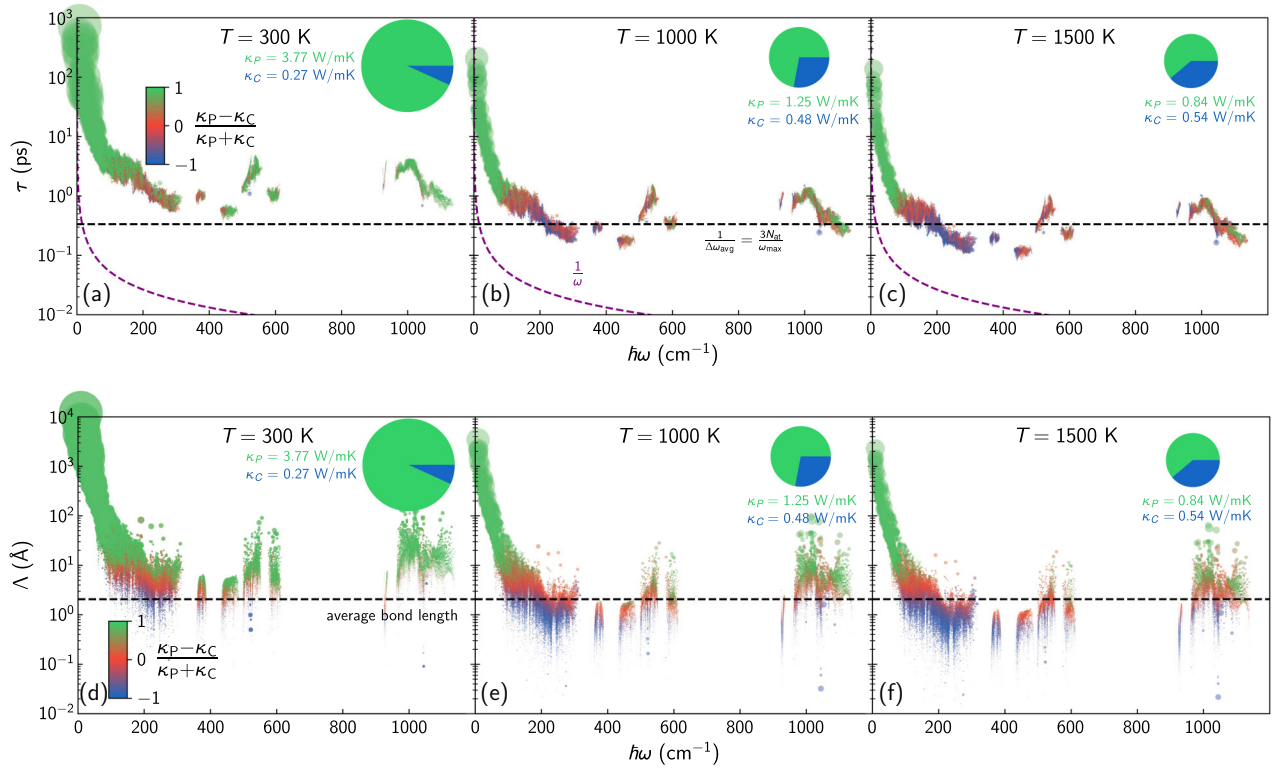
FIG. 4. Phonon lifetimes (a)–(c) and mean free paths (d)–(f) as a function of energy at different temperatures. A color code has been used to show the origin of the conduction mechanism; green, blue, and red represent the particlelike, wavelike, and mixed conductivity (50% each), respectively. The area of each circle corresponds to its contribution to the total conductivity. In the upper panels, the horizontal black dashed line is the "Wigner limit in time," where the phonon lifetime $\tau(\mathbf{q})_s$ is equal to the inverse of the average interband spacing [$\tau(\mathbf{q})_s = [\Delta\omega_{\mathrm{avg}}]^{-1}$; see the text]. The purple dashed hyperbola $\tau = 1/\omega$ indicates the regime of validity of the Wigner formulation, which requires phonons above such a line to be well-defined (nonoverdamped) quasiparticles [84]. The horizontal dashed line in the mean free path panel is the average bond length of LaPO$_4$. The pie charts have an area proportional to the total conductivity; the green and blue slices represent the particlelike and wavelike contributions, respectively.

determined according to the value of the parameter

$$c = \frac{\bar{\mathcal{K}}_P(\mathbf{q})_s - \bar{\mathcal{K}}_C(\mathbf{q})_s}{\bar{\mathcal{K}}_P(\mathbf{q})_s + \bar{\mathcal{K}}_C(\mathbf{q})_s}. \qquad (5)$$

Equation (5) implies that $c = +1$ when the phonon $(\mathbf{q})_s$ predominantly contributes to particlelike conduction (corresponding to green), $c = -1$ when instead the phonon contributes mainly to wavelike conduction (blue), and, finally, $c = 0$ when the phonon contributes equally to particlelike and wavelike conduction (red). In the following, we employ a linear color scale interpolating blue, red, and green to resolve possible intermediate cases. The second piece of information, on the magnitude of the transport mechanisms, is represented by the area of each scatter point, which is proportional to the contribution of such phonon to the total thermal conductivity [size $\propto \bar{\mathcal{K}}_P(\mathbf{q})_s + \bar{\mathcal{K}}_C(\mathbf{q})_s$]. Figure 4 shows that the relative strength of particlelike and wavelike mechanisms strongly depends on the energy of the phonon, and varies

significantly with temperature. Specifically, at room temperature (panel (a)), most of the phonons have a lifetime $\tau(\mathbf{q})_s$ above the Wigner limit in time $[\Delta\omega_{\mathrm{avg}}]^{-1}$ (represented by the horizontal black dashed line), and their green color indicates that they mainly contribute to particlelike transport. Increasing temperature (panel (b) is 1000 K, and panel (c) is 1500 K) yields a reduction of the lifetimes; numerical results confirm the analytical expectations that phonons with a lifetime comparable to the Wigner limit in time (red) contribute simultaneously to particlelike and wavelike conduction mechanisms, and phonons with even shorter lifetimes mainly contribute to wavelike transport. These findings can be intuitively understood by recalling that phonons with extremely short lifetime are suppressed very quickly and thus cannot propagate particlelike enough to yield a sizable contribution to the populations conductivity. However, these short-lived phonons can still interfere and tunnel wavelike—we recall that interference and tunneling also occur between damped waves—resulting in a significant contribution to the wavelike conductivity. Finally, we highlight that all the phonons in LaPO$_4$ have

lifetimes longer than their reciprocal frequencies [$\tau(\mathbf{q})_s > [\omega(\mathbf{q})_s]^{-1}$, i.e., they are all above the purple dashed line in panels (a)–(c)]; thus, Landau's quasiparticle picture [84] for phonons holds in LaPO$_4$ and consequently the Wigner formulation can be applied [33,40].

The lifetime-energy analysis reported in the upper panel of Fig. 4 sheds light on the microscopic timescales underlying heat transport, and how they affect the macroscopic conductivity. In order to gain further insights, particularly on the dependence of the conductivity on the grains' length scales discussed in the previous section, it is useful to recast such an analysis in the space-energy domain. To achieve this, we multiply the phonon lifetimes by the corresponding group velocities, obtaining the microscopic propagation length scales of phonons [mean free paths (MFPs)] $\Lambda(\mathbf{q})_s = \|v(\mathbf{q})_{ss}\|\tau(\mathbf{q})_s/\sqrt{3}$ [here, $\|v(\mathbf{q})_{ss}\|/\sqrt{3}$ is the spatially averaged modulus of the group velocity].

The bottom panels of Fig. 4 show the MFP versus phonon energy at 300 K (d), 1000 K (e), and 1500 K (f). Similarly to the phonon lifetime-energy plots, a crossover from particlelike to wavelike transport is clearly evident here as well, and such a nonsharp transition is centered around the average bond length (see Ref. [33] for details on the relation between the particle-wave crossover in space and the average bond length). We highlight how phonons with MFPs larger (smaller) than the average bond length contribute to particle (wavelike) conduction, and phonons with MFPs equal to the average bond length contribute simultaneously to both particle and wave mechanisms. Finally, we note from the lower panels of Fig. 4 that it is apparent that most of the phonons in LaPO$_4$ have MFPs always equal or shorter than 1 μm, rationalizing the small difference between the bulk thermal conductivity and the thermal conductivity computed having accounted for grain-boundary scattering at length scale 1 μm discussed in Fig. 3.

D. Engineering the thermal conductivity through compositional disorder

1. Effects of compositional disorder on vibrational properties

La$_{1-x}$Gd$_x$PO$_4$ alloys are promising materials for future thermal barrier applications, due to their excellent thermal stability and chemical durability [85]. In general, the presence of compositional disorder (alloying) causes a reduction of the thermal conductivity [1,2,31,32,86–92], and is thus expected to be beneficial for TBC applications. To the best of our knowledge, there are no theoretical or experimental works on the thermal conductivity of La$_{1-x}$Gd$_x$PO$_4$ alloys. As anticipated in the Introduction, recent work [32] has highlighted how the standard LBTE-based perturbative treatment of compositional disorder [29,30,86]—which is accurate in systems with weak disorder or weak anharmonicity and low-frequency (acoustic) vibrational modes

dominating transport [30,31,86]—fails in systems where transport is not dominated by low-frequency modes. We have seen in Fig. 4 that LaPO$_4$ at high temperature belongs to this class; hence, in this section we develop a computational protocol that exploits the Wigner formulation to describe compositional-mass disorder explicitly, overcoming the limitations of the standard LBTE-based perturbative treatment of disorder. In particular, the perturbative treatment of mass disorder introduced by Tamura [29] for isotopic impurities is limited to describing how weak compositional disorder affects the phonon linewidths and the particlelike conductivity emerging from the LBTE. Here we overcome the limitations of such a perturbative description by introducing an approach that can be applied to systems with arbitrary disorder and anharmonicity. We show that this approach explicitly accounts for the effect of compositional (mass) disorder on thermal transport, comprehensively describing how disorder affects the vibrational frequencies, velocity operator, and intrinsic anharmonic linewidths that determine the particlelike and wavelike conductivities.

To explicitly describe how compositional-mass disorder affects the conductivity, we need to compute the quantities entering Eq. (1)—i.e., vibrational frequencies, velocity operators, and linewidths—in compositionally disordered structures. Starting from the harmonic frequencies and velocity operators, we compute them explicitly in the mass-substitution approximation [65] according to the following procedure: (i) we build a perfect supercell (of size up to 6 × 6 × 6, i.e., containing up to 5184 atoms) of the primitive cell of LaPO$_4$; (ii) we destroy the crystalline order within such a supercell by introducing compositional disorder (hereafter we use the term "disordered cell" to refer to this compositionally disordered atomic structure); (iii) we calculate the vibrational properties of the disordered cell. In particular, in step (ii) we introduce compositional disorder in the rare-earth site by replacing the mass of La with that of Gd with probability $x \in [0, 1]$ in the mass-rescaled force-constant tensor:

$$G_{\mathbf{R}b\alpha,\mathbf{R}'b'\alpha'} = \frac{1}{\sqrt{f_x(M_b)f_x(M_{b'})}} \frac{\partial^2 V}{\partial u(\mathbf{R})_{b\alpha}\partial u(\mathbf{R}')_{b'\alpha'}}\bigg|_{\text{eq}}. \quad (6)$$

Here $\mathbf{R}$ is a Bravais vector, b denotes an atom having mass M_b and position in the primitive cell $\boldsymbol{\tau}_b$, and α is a Cartesian direction; $\partial^2 V/\partial u(\mathbf{R})_{b\alpha}\partial u(\mathbf{R}')_{b'\alpha'}|_{\text{eq}}$ is the second derivative of the Born-Oppenheimer potential evaluated at equilibrium atomic positions, which within the mass-substitution approximation [65] is considered to be equal to that of pure LaPO$_4$. The function f_x introduces compositional-mass disorder on the La sites by replacing the mass of La with that of Gd with probability

$x \in [0, 1]$, i.e.,

$$f_x(M_{La}) = \begin{cases} M_{La} & \text{with probability } 1 - x, \\ M_{Gd} & \text{with probability } x, \end{cases} \quad (7)$$

while it leaves unaffected the masses of O and P [$f_x(M_O) = M_O$ and $f_x(M_P) = M_P$ for all x]. Then, the disordered harmonic mass-rescaled force-constant tensor (6) is used to compute the dynamical matrix at wave vector **q**,

$$D(\mathbf{q})_{b\alpha,b'\alpha'} = \sum_{\mathbf{R}} G_{\mathbf{R}b\alpha,\mathbf{0}b'\alpha'} e^{-i\mathbf{q}\cdot(\mathbf{R}+\tau_b-\tau_{b'})}, \quad (8)$$

which is then diagonalized,

$$\sum_{b'\alpha'} D(\mathbf{q})_{b\alpha,b'\alpha'} \mathcal{E}(\mathbf{q})_{s,b'\alpha'} = \omega^2(\mathbf{q})_s \mathcal{E}(\mathbf{q})_{s,b\alpha}. \quad (9)$$

The eigenvalues appearing in Eq. (9) are related to the vibrational frequencies $\omega(\mathbf{q})_s$, and the eigenvectors $\mathcal{E}(\mathbf{q})_{s,b\alpha}$ describe how atom b moves along the Cartesian direction α when the phonon with wave vector **q** and mode s is excited. As discussed in Ref. [33], the velocity operator is obtained from these quantities as

$$v^{\beta}(\mathbf{q})_{s,s'} = \sum_{b\alpha,b'\alpha'} \mathcal{E}^{\star}(\mathbf{q})_{s,b\alpha} \left(\nabla_{\mathbf{q}}^{\beta} \sqrt{D(\mathbf{q})}_{b\alpha,b'\alpha'} \right) \mathcal{E}(\mathbf{q})_{s',b'\alpha'}. \quad (10)$$

To estimate the effect of compositional disorder on the linewidths, we focus on bulk systems with negligible (zero) grain-boundary linewidths. In addition, we neglect intrinsic isotopic impurity disorder, since it has negligible effects on the conductivity of LaPO$_4$ and GdPO$_4$ (see Fig. 13 in Appendix E). To evaluate the effect of compositional disorder on the dominant, anharmonic part of the linewidths $\hbar\Gamma^{anh}(\mathbf{q})_s$, we calculate such a quantity [Eq. (A1) in Appendix A] using third-order force constants modified to account for compositional disorder using the aforementioned mass-replacement function $f(M_b)$ [see Eq. (A2) in Appendix A].

We show in Fig. 5 that the mass-substitution approximation captures the lower conductivity of pure GdPO$_4$ compared to pure LaPO$_4$, in agreement with experiments (see Refs. [46,93] for the former, and Refs. [46–49] for the latter). Therefore, the mass-substitution approximation is accurate enough for the scope of the present analysis. The inset of Fig. 5 shows that GdPO$_4$ has conductivity lower than LaPO$_4$ because of a simultaneous reduction of both the particlelike and wavelike conductivities. The reduction of κ_P caused by the substitution La→Gd can be understood from the increase in the linewidth shown in Fig. 10 in Appendix B, and the reduction of the energy of the acoustic modes (i.e., reduction in the phonon group velocities)
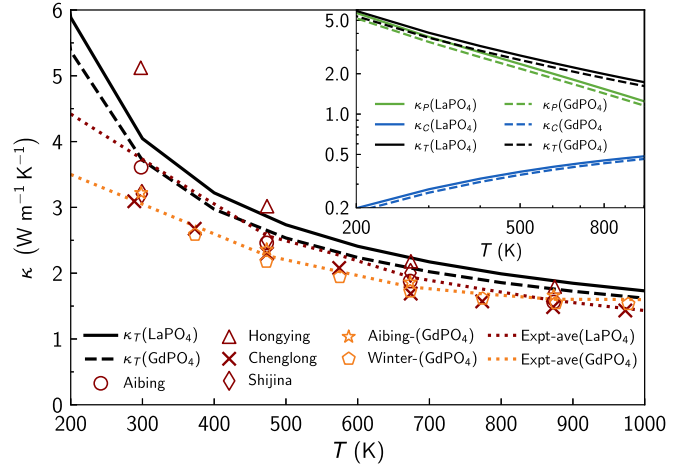

FIG. 5. Conductivities of pure LaPO$_4$ and GdPO$_4$. The total conductivity of LaPO$_4$ (GdPO$_4$) is shown with a black solid (dashed) line, and experiments with red [46–49] (orange [46,93]) symbols. The red dotted (orange) line is the average of the experimental data for LaPO$_4$ (GdPO$_4$). Inset: the reduction of the total conductivity (κ_T) caused by completely replacing La→Gd originates from a simultaneous reduction of particlelike (κ_P) and wavelike (κ_C) conductivities.

shown in Fig. 16(c) in Appendix F. The reduction of κ_C upon La→Gd substitution is caused by the decrease of the off-diagonal velocity-operator elements, which accompanies the decrease of the group velocities (diagonal velocity-operator elements).

Knowledge of the anharmonic linewidths of pristine LaPO$_4$ and GdPO$_4$ (see Fig. 10 in Appendix B; both these pristine materials have a 24-atom primitive cell), and the unaffordable computational cost for calculating of the anharmonic linewidths in disordered cells of La$_{1-x}$Gd$_x$PO$_4$ containing thousands of atoms [44], motivate us to adopt the approximate description of anharmonic linewidths for alloys introduced in past work [32,44,86]. In practice, this corresponds to (i) coarse graining the frequency-anharmonic-linewidth distributions of pure LaPO$_4$ and pure GdPO$_4$ into single-valued functions of ω, $\Gamma^{anh}_{LaPO_4}(\omega)$ and $\Gamma^{anh}_{GdPO_4}(\omega)$ [Appendix B discusses the use of Eq. (B1) for such coarse graining, and the accuracy of the approximations performed]; (ii) determining the linewidths of the disordered alloy by the composition-weighted average of the LaPO$_4$ and GdPO$_4$ linewidths [94]:

$$\Gamma^{anh}_{La_{1-x}Gd_xPO_4}(\omega) = (1-x)\Gamma^{anh}_{LaPO_4}(\omega) + x\,\Gamma^{anh}_{GdPO_4}(\omega). \quad (11)$$

2. Effects of compositional disorder on thermal properties

After having computed the harmonic frequencies and velocity operators, and anharmonic linewidths in a compositionally disordered cell with Eq. (11), we use

these quantities to evaluate the thermal conductivity (1). Implementation details of this protocol are provided in Appendix F 3.

The description of how compositional disorder affects thermal conductivity becomes more accurate as one increases the size of the disordered cell. In practice, one has to numerically verify that the disordered cell is large enough to yield computational convergence; this can be done by computing all the parameters entering Eq. (1) in increasingly larger disordered cells, and verifying that, for sizes larger than a certain value, the conductivity remains practically unchanged. In Fig. 6 we test the computational convergence for the case $x = 0.5$, where we show that employing disordered cells containing 1536, 3000, and 5184 atoms yields practically indistinguishable results for the total conductivity. It is worth noting that in these calculations we used Fourier interpolation to improve the accuracy with which bulk vibrational and thermal properties are extrapolated from the finite atomistic model [44,95,96]. In particular, we computed these properties using a $5 \times 5 \times 5$ **q** mesh for the 1536-atom cell, a $3 \times 3 \times 3$ **q** mesh for the 3000-atom cell, and a $3 \times 3 \times 3$ **q** mesh for the 5184-atom

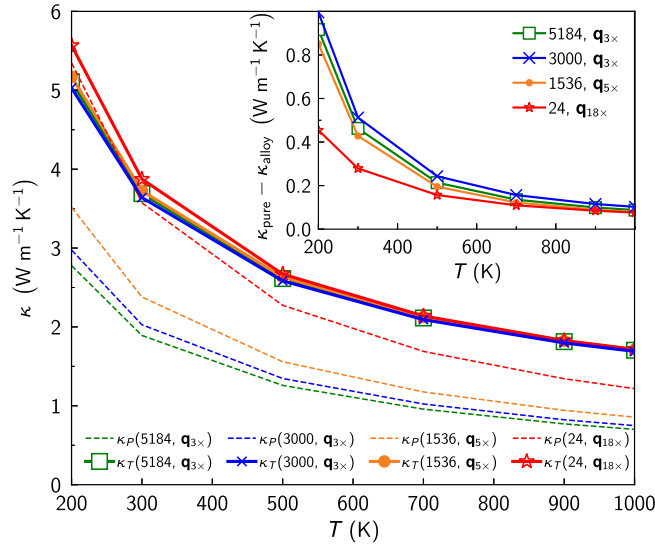FIG. 6. Thermal conductivity of models of $La_{0.5}Gd_{0.5}PO_4$ having different sizes. The solid lines with the markers are total conductivities κ_T; dashed lines are the particlelike conductivities κ_P. Different colors denote calculations done in disordered cells having different sizes and using different **q** meshes (in the legend, numbers represent the numbers of atoms in the disordered cells, and "$\mathbf{q}_{n\times}$" means that conductivities are evaluated on a $n \times n \times n$ **q** mesh). The particlelike conductivity κ_P decreases as the size of the model increases; also accounting for the wavelike conductivity κ_C in models containing 1536 or more atoms atoms, the total conductivity $\kappa_T = \kappa_P + \kappa_C$ converges to the bulk (size-independent) limit of the conductivity $\kappa_T = \kappa_P + \kappa_C$. Inset: difference between the total conductivity of pure $LaPO_4$ and that of $La_{0.5}Gd_{0.5}PO_4$ described with disordered cells containing 24, 1536, 3000, and 5184 atoms.

cell. We recall that performing a Fourier interpolation on a $n \times n \times n$ **q** mesh spanning the Brillouin zone of a certain reference cell allows us to simulate a system that is $n \times n \times n$ larger, but with a disorder length scale limited to the size of the reference cell [44,45,97]. Therefore, comparing calculations performed using disordered cells of different sizes, and using different meshes, provides information about how much the conductivity is affected by finite-size effects. Figure 6 shows that the total conductivities obtained from disordered atomistic models having cell size (i.e., disorder length scales) ranging from 1536 to 5184 atoms are practically indistinguishable in the **q**-sampling limit [98]; this implies that, for $La_{1-x}Gd_xPO_4$ alloys, disordered cells containing 1536 atoms are already sufficiently large to yield a computationally converged value for the thermal conductivity.

Figure 6 also highlights that, in order to predict the bulk limit of the thermal conductivity of an alloy, it is necessary to (i) account for both particlelike and wavelike transport mechanisms via Eq. (1); (ii) evaluate Eq. (1) using compositionally disordered cells of size sufficiently large to accurately describe disorder. These two requirements are related. In fact, introducing compositional disorder in $LaPO_4$ causes a reduction of κ_P [99] and an increase of κ_C. We find that in $La_{1-x}Gd_xPO_4$ alloys, upon increasing the size of the disordered cell (i.e., accuracy in the description of disorder) beyond 1536 atoms, the total Wigner conductivity $\kappa_T = \kappa_P + \kappa_C$ converges to a size-independent, bulk limit of the alloy's conductivity (see the inset of Fig. 6 and Fig. 7).

As already discussed in Refs. [86,95], in the presence of disorder the particlelike conductivity depends on the size of the disordered cell used to describe the system, and converges to zero in the limit of infinitely large disordered cells. This last statement is supported by numerical evidence in Fig. 7, Fig. 4.7 of Ref. [86], and Fig. 12 of Ref. [44], and additional details are provided in Appendix D. To further confirm and validate that the reduction of the conductivity is caused by compositional disorder, we verified that in a pristine $LaPO_4$ crystal without disorder κ_P, κ_C, and κ_T are all independent from the arbitrary choice of the crystal's unit cell: the dashed lines in Fig. 7 demonstrate this for cells containing 24 atoms (primitive cell), 1536 atoms ($4 \times 4 \times 4$ supercell), and 5184 atoms ($6 \times 6 \times 6$ supercell); Fig. 12 in Appendix D shows analogous tests performed at higher temperatures.

After having validated the computational protocol to describe disorder in the mass-substitution approximation within the Wigner framework, we analyze how the variable compositional disorder affects thermal conductivity. Figure 8 shows the conductivity of $La_{1-x}Gd_xPO_4$ alloys at different compositions and various temperatures. We see that, compared to pristine $LaPO_4$, the conductivity decreases as compositional disorder increases. Such a decrease is more pronounced at low temperatures (300 K),
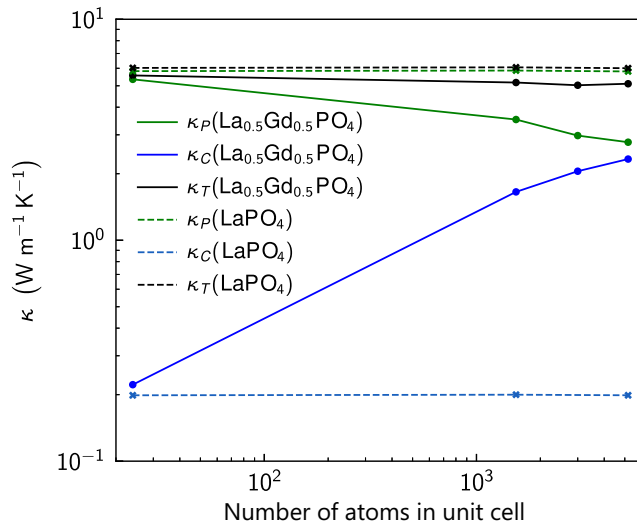
FIG. 7. Necessity to consider both κ_P and κ_C to describe the thermal conductivity of alloys. Green, blue, and black are particlelike (κ_P), wavelike (κ_C), and total ($\kappa_T = \kappa_P + \kappa_C$) conductivities at 200 K for pristine $LaPO_4$ (dashed) and $La_{0.5}Gd_{0.5}PO_4$ alloy (solid). We highlight how, when the alloy is accurately described with large disordered cells, the total conductivity κ_T respects the physical expectation of being independent from the number of atoms in the alloy's unit cell, even if the ratio κ_P/κ_C is size dependent [44].

where anharmonicity is weak and does not dominate over disorder in limiting heat transfer. At 300 K, the dependence of the conductivity from composition bears analogies with that observed in other alloys [9,30,89,100–105], displaying a U-shaped trend that reaches a minimum at $x \sim 0.7$. We note that in the minimum the conductivity is about 12% lower than that of pristine $LaPO_4$. Such a decrease is much smaller than the order-of-magnitude decrease observed in archetypal alloys such as Si_xGe_{1-x} [30] for two reasons. First, anharmonicity in $LaPO_4$ and $GdPO_4$ is much stronger than that in Si and Ge, yielding a much lower thermal conductivity already in the pristine components; second, there is less mass contrast between La and Gd (mass ratio, Gd/La = 1.13) compared to Si and Ge (mass ratio, Ge/Si = 2.59). When increasing the temperature, anharmonic effects become stronger and thus progressively dominate over compositional disorder in determining the conductivity; this is apparent from the almost negligible dependence of the conductivity from compositional disorder (and disappearance of the U-shaped trend) observed at 1000 K.

In summary, we have developed a computational protocol that allows us to evaluate the effect of compositional disorder within the Wigner framework. This protocol allows us to shed light on how the interplay between compositional disorder and anharmonicity determines the conductivity, and will be potentially very useful to study materials for next-generation TBCs.
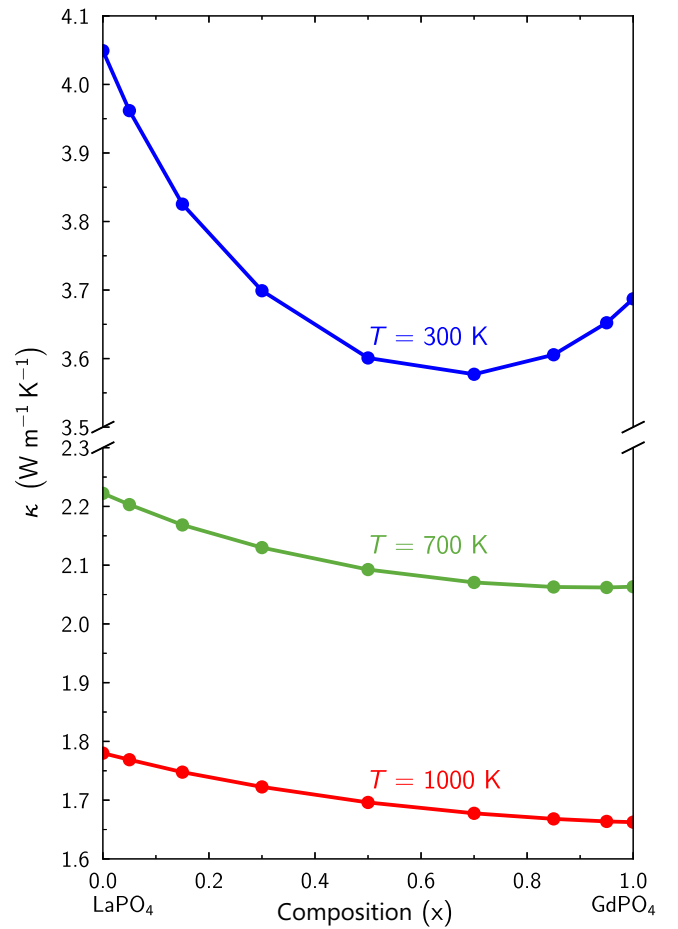

FIG. 8. Thermal conductivity of $La_{1-x}Gd_xPO_4$ alloys as a function of composition, at 300, 700, and 1000 K. At 300 K, the conductivity drops as compositional disorder increases, reaching a minimum at $x \sim 0.7$. The effect of compositional disorder becomes less relevant as temperature increases.

3. Micrometer-scale disorder: $LaPO_4/La_2Zr_2O_7$ composites

$La_2Zr_2O_7$ has been identified as another potential TBC material with very low thermal conductivity [7]. However, its low thermal expansion coefficient causes the formation of cracks and delamination at high temperatures [106]. Composite structures of $La_2Zr_2O_7$ and $LaPO_4$ have been suggested to offer better thermomechanical properties compared to the base materials [81]. Computing the thermal conductivity of composites characterized by compositional disorder at the micrometer length scale has a prohibitively high computational cost for first-principles methods. Therefore, in order to have a qualitative understanding of heat conduction in $LaPO_4/La_2Zr_2O_7$ composites, we employ the continuum Maxwell [54] model for the effective conductivity of a composite (see Eq. 2.14 of Ref. [55]), which determines the total thermal conductivity of the composite (κ_{mix}) from the total conductivities of the
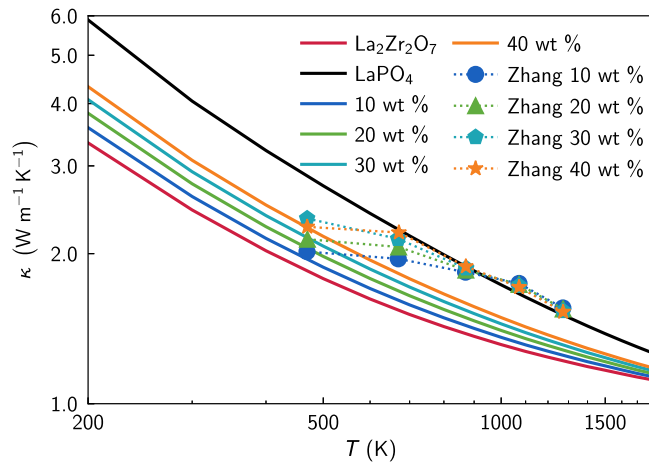
FIG. 9. Conductivity of $LaPO_4$/$La_2Zr_2O_7$ composites. $LaPO_4$ (filler) is added to $La_2Zr_2O_7$ (matrix) at different weight percentages, and the thermal conductivity is computed using Maxwell's effective-conductivity model for composites [54,55]. Experimental data are taken from Zhang *et al.* [81].

matrix (κ_1) and filler (κ_2):

$$\frac{\kappa_{\mathrm{mix}} - \kappa_1}{\kappa_{\mathrm{mix}} + 2\kappa_1} = V \frac{\kappa_2 - \kappa_1}{\kappa_2 + 2\kappa_1} \qquad (12)$$

with V the volume fraction of the filler. Here we consider $La_2Zr_2O_7$ as the matrix (its conductivity is taken from ref [33]) and $LaPO_4$ as the filler. As in the experimental work by Zhang *et al.* [81], we consider composites containing weight percentages $LaPO_4$ equal to 10%, 20%, 30%, and 40%, and we estimate the conductivity of the composite using Eq. (12). Figure 9 shows the thermal conductivity of the composite as a function of temperature at different filler fractions. The conductivity increases with an increase in the fraction of $LaPO_4$; in all cases, it is higher than that of pristine $La_2Zr_2O_7$ and smaller than that of $LaPO_4$. This trend is in broad agreement with the experiments performed by Zhang *et al.* [81]. We also note that experimental samples have porosities that vary with the filler fraction, as well as interfaces between $La_2Zr_2O_7$ and $LaPO_4$ phases. These effects are not accounted for by Maxwell's effective-conductivity model employed here, and their description might improve the agreement between theory and experiments in Fig. 9, but it is an open challenging problem that is beyond the scope of the present paper.

IV. CONCLUSIONS

We have shown that the Wigner formulation of thermal transport [33] can be combined with first-principles techniques to quantitatively predict the macroscopic thermal-insulation performance of compositionally disordered materials for thermal barrier coatings [2–5,85]. First, we have investigated heat transport in pristine $LaPO_4$, showing that the recently developed Wigner transport equation

[28,33] rationalizes the conductivity decay milder than T^{-1} observed in experiments [46–49]. More precisely, we have shown that the macroscopic trend of the conductivity is determined by the coexistence of microscopic particlelike and wavelike conduction mechanisms: the former strongly decays with temperature, while the latter increases with temperature, and the sum of the two yields the mildly decreasing trend observed in experiments. We have discussed how grain-boundary scattering affects the conductivity of $LaPO_4$, showing that such a mechanism has a weak effect in samples having micrometric grains, but would become very important in nanostructured samples [82,83]. In particular, we have analyzed how the relative strength of particlelike and wavelike transport mechanisms depends on the temperature, energy, and mean free path of the microscopic heat carriers. We have developed and tested a computational protocol that allows us to explicitly describe within the Wigner formulation how compositional disorder affects the conductivity, and we employed it to investigate the thermal properties of $La_{1-x}Gd_xPO_4$ alloys. In particular, we described compositionally disordered samples containing up to 5184 atoms, a size that is one order of magnitude larger than that tractable by state-of-the-art first-principles molecular dynamics techniques. We discussed how the interplay between anharmonicity and disorder affects thermal transport in $La_{1-x}Gd_xPO_4$ alloys at different temperatures, showing that disorder has strong effects around room temperature and almost negligible effects at high temperatures ($\gtrsim 700$ K). We have gained two important insights into the problem of predicting the thermal conductivity of alloys with nonperturbative compositional disorder (i.e., described explicitly with disordered cells containing thousands of symmetry-inequivalent atoms). First, we have confirmed the inadequacy of the particlelike LBTE in addressing such a problem, as it would predict a conductivity converging to zero upon increasing the size of the disordered cell [86]. Second, and most importantly, we have shown that the Wigner transport equation successfully addresses this problem, as it describes how in alloys the total conductivity, obtained as the sum of the particlelike and wavelike conductivities, converges to the size-independent bulk limit of the conductivity. The computational scheme introduced here sets the stage to rationalize thermal transport with quantum accuracy in solids with compositional-mass disorder, and will be potentially very useful to develop novel design strategies for thermal barrier coatings.

The raw data needed to reproduce the findings of this study are available on the Materials Cloud Archive [107].

APPENDIX A: PHONON LINEWIDTHS

The linewidths appearing in Eq. (1) are determined by third-order anharmonicity [18,59], isotopic impurity disorder [18,29], and grain-boundary scattering [60,61]. Specifically, the anharmonic linewidth is

$$
\hbar\Gamma^{\mathrm{anh}}(\mathbf{q})_s = \frac{\pi}{\hbar N_c} \sum_{\mathbf{q}',s',s''} |V^{(3)}_{\mathbf{q}s,\mathbf{q}'s',\mathbf{q}''s''}|^2 \{[1 + \bar{N}(\mathbf{q}')_{s'} + \bar{N}(\mathbf{q}'')_{s''}]\delta[\omega(\mathbf{q})_s - \omega(\mathbf{q}')_{s'} - \omega(\mathbf{q}'')_{s''}]
$$
$$
+ 2[\bar{N}(\mathbf{q}')_{s'} - \bar{N}(\mathbf{q}'')_{s''}]\delta[\omega(\mathbf{q})_s + \omega(\mathbf{q}')_{s'} - \omega(\mathbf{q}'')_{s''}]\}, \tag{A1}
$$

where

$$
V^{(3)}_{\mathbf{q}s,\mathbf{q}'s',\mathbf{q}''s''} = \sum_{\substack{\alpha,\alpha',\alpha'' \\ b,b',b''}} \mathcal{E}(\mathbf{q})_{s,b\alpha}\mathcal{E}(\mathbf{q}')_{s',b'\alpha'}\mathcal{E}(\mathbf{q}'')_{s'',b''\alpha''} \sqrt{\frac{1}{f_x(M_b)f_x(M_{b'})f_x(M_{b''})}} \sqrt{\frac{\hbar^3}{8}} \sqrt{\frac{1}{\omega(\mathbf{q})_s\omega(\mathbf{q}')_{s'}\omega(\mathbf{q}'')_{s''}}}
$$
$$
\times \frac{1}{N_c} \frac{\partial^3 V}{\partial u(\mathbf{q})_{b\alpha}\partial u(\mathbf{q}')_{b'\alpha'}\partial u(\mathbf{q}'')_{b''\alpha''}} \tag{A2}
$$

are the three-phonon coupling matrix elements [59] and $f_x(M_b)$ is the mass-replacement function used to account for compositional disorder in the mass-substitution approximation discussed in Sec. III D 1. The linewidth due to isotopic impurity disorder (used only in the pure cases) is [18,29]

$$
\hbar\Gamma^{\mathrm{imp}}(\mathbf{q})_s = \frac{\hbar\pi}{2N_c}[\omega(\mathbf{q})_s]^2 \sum_{\mathbf{q}',s'} \delta[\omega(\mathbf{q})_s - \omega(\mathbf{q}')_{s'}] \sum_b g_2^b \left| \sum_\alpha \mathcal{E}(\mathbf{q})^\star_{s,b\alpha}\mathcal{E}(\mathbf{q}')_{s',b\alpha} \right|^2, \tag{A3}
$$

where $g_2^b = \sum_i f_{i,b}([\langle m_b \rangle - m_{i,b}]/\langle m_b \rangle)^2$ is the mass-variance parameter for the masses of atom b ($f_{i,b}$ and $m_{i,b}$ are the mole fraction and mass, respectively, of the ith isotope of atom b; $\langle m_b \rangle = \sum_i f_{i,b}m_{i,b}$ is the weighted average mass).

Finally, the linewidth due to grain-boundary scattering evaluated according to the Casimir model [61] in the presence of perfectly absorbing boundaries is [60]

$$
\hbar\Gamma(\mathbf{q})^{\mathrm{bnd}}_s = \frac{\|v(\mathbf{q})_{ss}\|}{L}. \tag{A4}
$$

APPENDIX B: REPRESENTING ANHARMONIC LINEWIDTHS AS A FUNCTION OF FREQUENCY

In this section, we discuss the details of the computation of the analytical function $\Gamma^{\mathrm{anh}}(\omega)$, used in Sec. III D 1 to approximatively determine the linewidths as a function of frequency. Similarly to previous work [32,44,86], the description of anharmonic linewidths as a single-value function of frequency, $\Gamma^{\mathrm{anh}}(\omega)$, is determined as

$$
\Gamma^{\mathrm{anh}}(\omega) = \frac{1}{\sqrt{1/\Gamma_1(\omega)^2 + 1/\Gamma_2(\omega)^2}}, \tag{B1}
$$

where $\Gamma_1(\omega)$ and $\Gamma_2(\omega)$ are defined as

$$\Gamma_1(\omega) = \frac{\sum_{\mathbf{q},s} \frac{1}{\sqrt{2\pi\sigma^2}} \exp\left[-\frac{\hbar^2(\omega(\mathbf{q})_s - \omega)^2}{2\sigma^2}\right]}{\sum_{\mathbf{q},s} [\Gamma^{\mathrm{anh}}(\mathbf{q})_s]^{-1} \frac{1}{\sqrt{2\pi\sigma^2}} \exp\left[-\frac{\hbar^2(\omega(\mathbf{q})_s - \omega)^2}{2\sigma^2}\right]}, \tag{B2}$$

$$\Gamma_2(\omega) = p \cdot \omega^2, \tag{B3}$$

with

$$p = \frac{\sum_{\mathbf{q},s} \int_{\omega_0}^{2\omega_0} d\omega' \frac{\Gamma^{\mathrm{anh}}(\mathbf{q})_s}{\omega^2(\mathbf{q})_s} \frac{2.35}{\sqrt{2\pi\sigma^2}} \exp\left[-\frac{\hbar^2(\omega(\mathbf{q})_s - \omega')^2}{2\sigma^2}\right]}{\sum_{\mathbf{q},s} \int_{\omega_0}^{2\omega_0} d\omega' \frac{1}{\sqrt{2\pi\sigma^2}} \exp\left[-\frac{\hbar^2(\omega(\mathbf{q})_s - \omega')^2}{2\sigma^2}\right]}, \tag{B4}$$

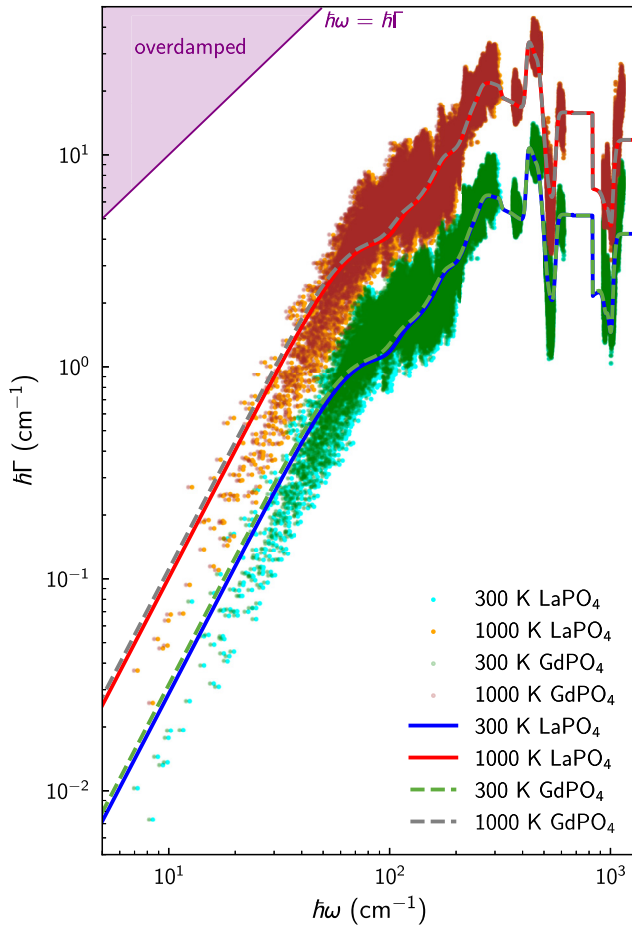FIG. 10. Frequency-anharmonic linewidth distribution of LaPO$_4$ and GdPO$_4$ at different temperatures, represented as scatter points. The lines show their coarse graining into single-valued functions $\Gamma^{\mathrm{anh}}(\omega)$; coarse-grained functions for LaPO$_4$ and GdPO$_4$ are shown with solid and dashed lines, respectively. The purple area is the overdamped regime, where the Wigner formulation cannot be applied.

ω_0 the smallest nonzero frequency, and $\sigma = 15$ cm^{-1} a broadening chosen sufficiently large to ensure that the linewidths are averaged in a smooth way. The functional form of the approximated function $\Gamma^{\mathrm{anh}}(\omega)$ is inspired by past work [32,44,86] and the specific expressions [(B1), (B2), (B3), (B4)] to determine it have been devised and validated relying on exact calculations performed in pure LaPO$_4$. Specifically, we show in Fig. 10 the function $\Gamma_{\mathrm{LaPO_4}}(\omega)$ for pure LaPO$_4$. In Fig. 11 we demonstrate that the exact and approximated treatments of anharmonicity yield practically indistinguishable conductivities over the entire temperature range analyzed.
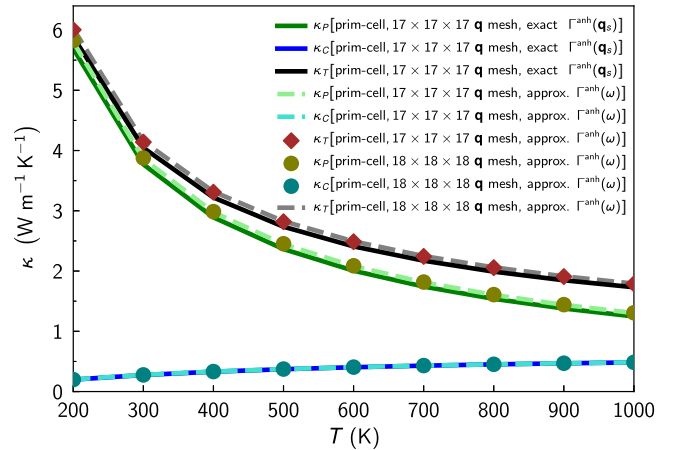

FIG. 11. Validation of the approximated treatment of anharmonicity. In LaPO$_4$ the κ_P, κ_C, and κ_T conductivities computed using the primitive cell and a $17 \times 17 \times 17$ **q** mesh remain practically unchanged if the exact linewidths (solid) or approximated linewidths [dashed; see Eq. (B1)] are used. Using the primitive cell and a $18 \times 18 \times 18$ **q** mesh, which contains exactly the same frequencies of a perfect $6 \times 6 \times 6$ supercell with a $3 \times 3 \times 3$ **q** mesh (see Fig. 12) yields conductivities (scatter points) compatible with the exact ones.

APPENDIX C: SINGLE-VIBRATION CONTRIBUTION TO THE PARTICLELIKE AND WAVELIKE CONDUCTIVITIES

In this appendix we report the full expression for the contribution of a vibration with wave vector $\mathbf{q}$ and mode s to the average trace of the particlelike and wavelike conductivity tensors [$\bar{\mathcal{K}}_P(\mathbf{q})_s$ and $\bar{\mathcal{K}}_C(\mathbf{q})_s$, respectively]. These single-mode conductivity contributions are used to compute the size of the points in Fig. 4 [size $\propto \bar{\mathcal{K}}_P(\mathbf{q})_s + \bar{\mathcal{K}}_C(\mathbf{q})_s$] and their color [Eq. (5)]. We note that this analysis could be extended to resolve Cartesian-direction-dependent contributions to the conductivity; here we consider the average over the three Cartesian directions for simplicity.

The expression for $\bar{\mathcal{K}}_P(\mathbf{q})_s$ follows directly from the average trace of the integrand of the SMRTA particlelike conductivity [30],

$$\kappa_{P,SMRTA}^{av} = \frac{1}{3}\sum_{\alpha=1}^{3}\frac{1}{\mathcal{V}N_c}\sum_{\mathbf{q},s}C(\mathbf{q})_s v^\alpha(\mathbf{q})_{s,s} v^\alpha(\mathbf{q})_{s,s}\frac{1}{\Gamma(\mathbf{q})_s},$$

(C1)

where $\mathcal{V}$ is the primitive-cell volume, N_c is the number of $\mathbf{q}$ points appearing in the sum, $C(\mathbf{q})_s$, $v^\alpha(\mathbf{q})_{s,s}$, and $\Gamma(\mathbf{q})_s$ are the specific heat, group velocity, and linewidths of the phonon $(\mathbf{q})_s$ already discussed in Sec. II. The contributions to the particlelike conductivity $\bar{\mathcal{K}}_P(\mathbf{q})_s$ are obtained from the terms entering the sum of Eq. (C1):

$$\bar{\mathcal{K}}_P(\mathbf{q})_s = C(\mathbf{q})_s \bar{V}^{av}(\mathbf{q})_{s,s} \bar{V}^{av}(\mathbf{q})_{s,s}[\Gamma(\mathbf{q})_s]^{-1} \quad (C2)$$

with $\bar{V}^{av}(\mathbf{q})_{s,s} = \sqrt{\frac{1}{3}\sum_{\alpha=1}^{3}|v^\alpha(\mathbf{q})_{s,s}|^2}$ the spatially averaged group velocity.

The expression for $\bar{\mathcal{K}}_C(\mathbf{q})_s$ is obtained starting from the average trace of the coherences conductivity tensor,

$$\kappa_C^{av} = \frac{1}{3}\sum_{\alpha=1}^{3}\frac{1}{\mathcal{V}N_c}\sum_{\mathbf{q},s\neq s'}\frac{\omega(\mathbf{q})_s + \omega(\mathbf{q})_{s'}}{4}\left[\frac{C(\mathbf{q})_s}{\omega(\mathbf{q})_s} + \frac{C(\mathbf{q})_{s'}}{\omega(\mathbf{q})_{s'}}\right]v^\alpha(\mathbf{q})_{s,s'}v^\alpha(\mathbf{q})_{s',s}\frac{[\Gamma(\mathbf{q})_s + \Gamma(\mathbf{q})_{s'}]/2}{[\omega(\mathbf{q})_{s'}-\omega(\mathbf{q})_s]^2 + [\Gamma(\mathbf{q})_s + \Gamma(\mathbf{q})_{s'}]^2/4}.$$

(C3)

The integrand of this equation contains couplings between pairs of vibrational modes. To resolve how much each single vibrational mode contributes to the pairwise wavelike (coherences) transport mechanism, we weight the contribution of each mode with its specific heat (see Ref. [33] for details), yielding the single-vibration contribution to the wavelike conductivity:

$$\bar{\mathcal{K}}_C(\mathbf{q})_s = \sum_{s'\neq s}\frac{C(\mathbf{q})_s}{C(\mathbf{q})_s + C(\mathbf{q})_{s'}}\frac{\omega(\mathbf{q})_s + \omega(\mathbf{q})_{s'}}{2}\left[\frac{C(\mathbf{q})_s}{\omega(\mathbf{q})_s} + \frac{C(\mathbf{q})_{s'}}{\omega(\mathbf{q})_{s'}}\right]$$

$$\times\left[\frac{1}{3}\sum_\alpha|v^\alpha(\mathbf{q})_{s,s'}|^2\right]\frac{[\Gamma(\mathbf{q})_s + \Gamma(\mathbf{q})_{s'}]/2}{[\omega(\mathbf{q})_{s'}-\omega(\mathbf{q})_s]^2 + [\Gamma(\mathbf{q})_s + \Gamma(\mathbf{q})_{s'}]^2/4}.$$

(C4)

APPENDIX D: STRENGTH OF PARTICLELIKE AND WAVELIKE TRANSPORT IN ORDERED OR DISORDERED CELLS

We show in Fig. 12 that in pristine LaPO$_4$, the particlelike, wavelike, and total conductivities do not depend on the arbitrary choice of the unit cell used to describe the system, in agreement with physical expectations.

We now provide an analytical reasoning that complements the numerical results reported in Sec. III D 2, which showed that in the presence of disorder the particlelike conductivity decreases upon increasing the size of the disordered cell used to describe the system (Figs. 6 and 7). This behavior can be understood analytically, recalling that (i) the conductivity of an extremely large disordered cell can be described without relying on Fourier interpolation [i.e., evaluating Eq. (1) at $\mathbf{q} = \mathbf{0}$ only, or over

an $n \times n \times n$ $\mathbf{q}$ mesh would produce no differences; see Ref. [44] for details]; (ii) the presence of disorder forbids degeneracies between vibrational modes [109]; (iii) due to time-reversal symmetry, the velocity operator at $\mathbf{q} = \mathbf{0}$ has zero diagonal elements. These properties imply that in the limiting case of an infinitely large disordered cell $\kappa_P = 0$, and only κ_C determines the total conductivity. To further confirm the correctness of this analytical reasoning, it is useful to apply it to the opposite limit of a perfect supercell of a pristine crystal. In this case, the vibrational frequencies at $\mathbf{q} = \mathbf{0}$ of the perfect supercell are simply obtained by folding the phonon bands of the primitive cell [110]. Then, the presence of crystal symmetries within the supercell allows for the emergence of perfectly degenerate vibrational modes, which contribute to the particlelike conductivity through nonzero off-diagonal-and-degenerate velocity-operator elements. These considerations imply
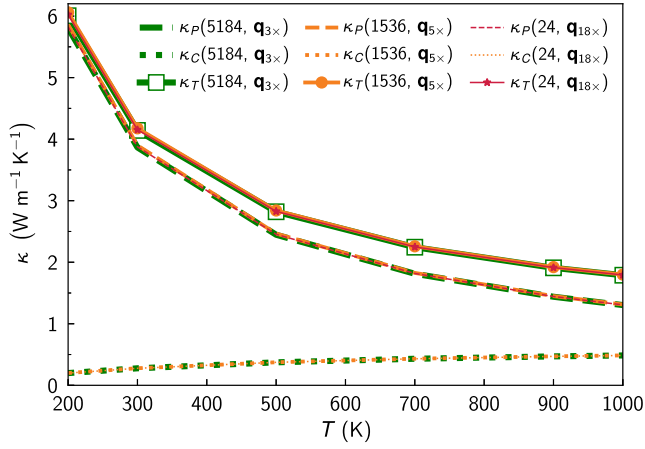
FIG. 12. Conductivity of pristine LaPO$_4$ described with different unit cells. The particlelike conductivity (κ_P, dashed, equivalent to the Peierls-Boltzmann conductivity), wavelike conductivity (dotted, κ_C), and total Wigner conductivity (solid, $\kappa_T = \kappa_P + \kappa_C$) are independent from the arbitrary choice of the unit cell used to describe a pristine crystal. Using the 24-atom primitive cell (red, evaluated on a $18 \times 18 \times 18$ **q** mesh), or supercells of the primitive containing a number of atoms equal to 1536 (orange, $4 \times 4 \times 4$ supercell, evaluated on a $5 \times 5 \times 5$ **q** mesh) and 5184 (green, $6 \times 6 \times 6$ supercell, evaluated on a $3 \times 3 \times 3$ **q** mesh), yields indistinguishable results.

that in pristine crystals κ_P, κ_C, and κ_T do not depend on the arbitrary choice of the unit cell used to describe the conductivity (see the dashed lines in Figs. 7 and 12, as well as Fig. 2 of Ref. [33]).

APPENDIX E: NEGLIGIBLE EFFECT OF ISOTOPES ON THE CONDUCTIVITY

In Fig. 13 we show that accounting or not for the contributions of isotopes to the linewidths [29] [Eq. (A3)] has negligible effects on the thermal conductivities of LaPO$_4$ and GdPO$_4$ (variations smaller than 1%).

APPENDIX F: COMPUTATIONAL METHODS

1. Structural and vibrational properties of LaPO$_4$

The crystal structure of monazite LaPO$_4$ is taken from the experimental work of Ni *et al.* [108]; it is monoclinic (space group $P2_1/n$) and contains 24 atoms (four formula units) in the primitive cell (Fig. 14).

DFT calculations are performed using the Quantum ESPRESSO (QE) distributions [111]. We employed the revised Perdew-Burke-Enzerhof functional (PBEsol) [112]; pseudopotentials were taken from the SSSP precision library (version 1.1.2) [113,114]. We used a kinetic energy cutoff of 80 Ry, and the Brillouin zone was sampled using a $3 \times 3 \times 3$ Monkhorst-Pack [115] k-point mesh with a (1 1 1) shift. The structure is relaxed using the variable cell relax (vc-relax) scheme, with a force convergence
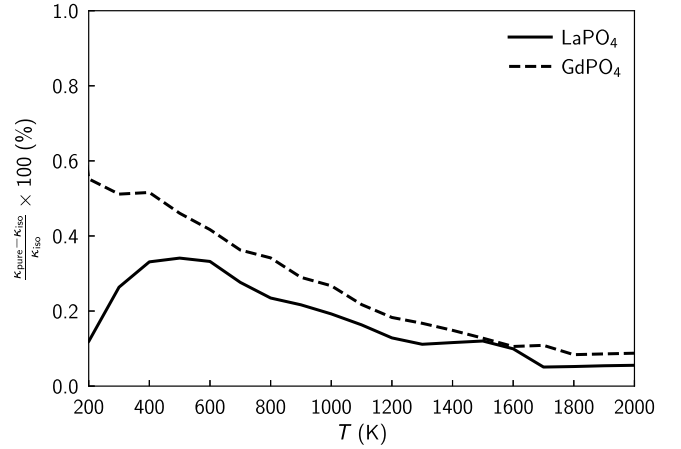

FIG. 13. Negligible effect of isotopes on conductivity. In pristine LaPO$_4$ (solid) and GdPO$_4$ (dashed), the relative difference between the total conductivity obtained whether or not accounting for isotopes at natural abundance [29] [$\kappa_{imp}(T)$ and $\kappa_{pure}(T)$, respectively] is always smaller than 0.6%.

threshold of 10^{-5} Ry/Bohr. The resulting equilibrium lattice parameters are in good agreement with experiments; see Table I.

The second-order force constants (fc2) are computed using density-functional perturbation theory [65] over a $4 \times 4 \times 4$ **q** mesh in reciprocal space. The LO-TO splitting at the Γ point is incorporated using the nonanalytic term correction computed with dielectric tensor and Born effective charges [116]. The absence of the imaginary phonon modes in the phonon dispersion (Fig. 15) confirms the dynamical stability.

The third-order force constants (fc3) are computed with a $2 \times 2 \times 2$ supercell using QE and the ShengBTE packages [117]. Here, the finite difference method is used and the nearest-neighbor interaction up to 8 nearest neighbors
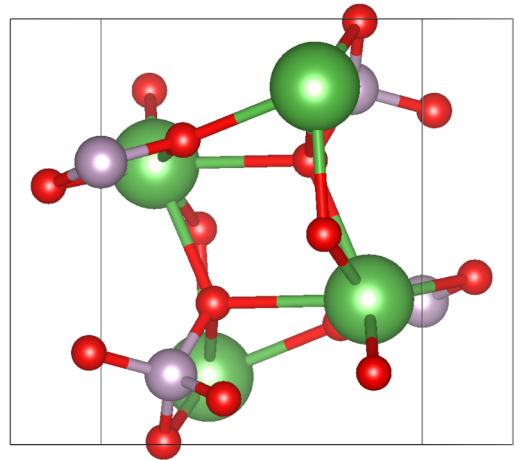

FIG. 14. DFT-optimized primitive cell of LaPO$_4$. Green, purple, and red represent La, P, and O atoms, respectively.

TABLE I.   Optimized lattice parameters and volume of LaPO$_4$. Experimental data are taken from Ni *et al.* [108]. The theoretical primitive-cell volume is 0.26% smaller than the experimental measurement at 300 K.

Functional	a (Å)	b (Å)	c (Å)	α (deg)	β (deg)	γ (deg)	V (Å^3)
PBEsol	6.843	7.074	6.478	90.000	103.478	90.000	304.938
Expt. from Ni *et al.* [108]	6.831	7.071	6.503	90.000	103.270	90.000	305.732

is incorporated. The QE fc2 and fc3 are exported to hdf5 formats using Phonopy [118] and HIPHIVE [119] packages, respectively. The linewidths are then computed using the Phono3py package [21,120].

2. Raman spectrum

The Raman intensities I_s appearing in Eq. (3) were computed from the Raman tensor [121,122]

$$\frac{\partial \chi_{ij}}{\partial u_{k,I}} = \frac{1}{\mathcal{V}} \frac{\partial^2 F_{k,I}}{\partial \mathcal{E}_i \partial \mathcal{E}_j}, \tag{F1}$$

where $F_{k,I}$ is the force acting on atom I and $\mathcal{E}$ is the macroscopic electric field. The Raman tensor was computed using the finite-electric-field approach [122], as implemented in the `aiida-vibroscopy` package [121] within the AiiDA infrastructure [123,124]. The second-order derivative appearing in Eq. (F1) was evaluated through the application of a small electric field, described by the electric enthalpy functional [125,126], an extension of the Kohn-Sham functional that allows us to find metastable solutions in the presence of a homogeneous electric field. In particular, we used a fourth-order central difference formula with an electric field step of about 0.8×10^{-3} (Ry) a.u. [1 (Ry) a.u. ≈ 36.3609 V/Å] to remove the finite size dependence of the numerical derivative (see Ref. [121] for details), and a Monkhorst-Pack grid of $10 \times 9 \times 10$ to ensure a well-converged spectra. Finally, the tensor was symmetrized according to the LaPO$_4$ space group.
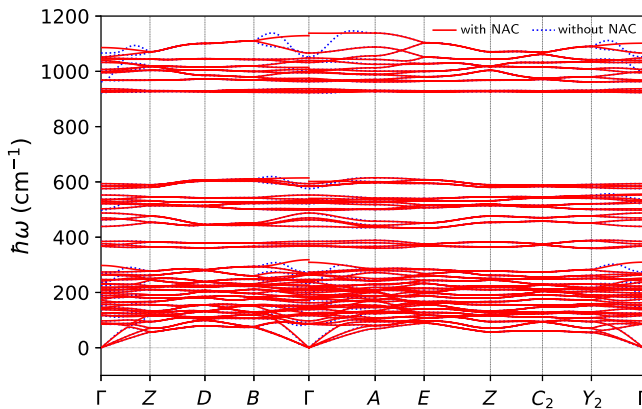

FIG. 15.   Phonon dispersion of LaPO$_4$. Red (blue) is with (without) the nonanalytic (NAC) term correction. We highlight how NAC affects the splitting of the LO-TO mode at $\mathbf{q} = \mathbf{0}$.

We conclude this appendix by discussing in more detail the temperature dependence of the Raman spectra in Fig. 1. Specifically, we note that the relative intensity of the theoretical Raman spectra does not decrease monotonically with temperature for all the peaks—the peak around 200 cm^{-1} is more intense at 1000 K than at 300 K. Such behavior originates from the presence of the temperature-independent instrumental linewidth in the Lorentzian (3), and from the Bose-Einstein distribution appearing in the Raman cross section for I_s. To quantitatively understand this behavior, we consider the maximum Raman intensity at $\omega \approx 200$ cm^{-1},

$$I(\omega = \omega_s, T) \sim [\bar{N}(\omega_s, T) + 1]/(\Gamma_s + \Gamma_{\text{ins}}), \tag{F2}$$

where $[\bar{N}(\omega_s, T) + 1] = (1 - \exp\{-\hbar\omega_s/k_B T\})^{-1}$. We see from Fig. 10 that, for $\omega_s \approx 200$ cm^{-1}, we have 2 cm$^{-1} = \Gamma_{\text{ins}} \gg \Gamma_s$. It follows that the temperature dependence of the Raman intensity of these modes arises entirely from the Bose-Einstein occupations. In particular, comparing the intensities at $T_1 = 300$ K and $T_2 = 1000$ K, we have

$$I(\omega_s, T_2)/I(\omega_s, T_1)$$
$$\approx [\bar{N}(\omega_s, T_2) + 1]/[\bar{N}(\omega_s, T_1) + 1] \approx 2.5, \tag{F3}$$

and this explains why the Raman peak at low-frequency becomes sharper upon increasing temperature. In contrast, for high-frequency modes, 2 cm$^{-1} = \Gamma_{\text{ins}} \ll \Gamma_s \sim T$, and from Eq. (F2), it follows that $[\bar{N}(\omega_s, T) + 1]/\Gamma_s$ decreases upon increasing temperature.

Finally, we note that the results reported in Fig. 1 are computed using the same level of theory used in the thermal conductivity calculations. Specifically, they are computed using the standard perturbative treatment of anharmonicity (also used in the phonon Boltzmann transport equation [74,127]) that considers third-order broadening effects (bubble three-phonon diagram) and neglects the renormalization of the frequencies due to anharmonicity and temperature. As discussed in Sec. V of Ref. [33], rigorously accounting for the influence of these effects on the thermal conductivity is an open challenging problem, which requires also accounting for anharmonic terms in the heat flux [128] to ensure a consistent treatment of the approximations that have to be performed.

3. Evaluating the Wigner conductivity of alloys

The thermal conductivity is calculated by solving the linearized form of the Wigner transport equation in the

homogeneous regime, relying on the solver implemented in the Phono3py code [120]. The scattering operator is computed on a mesh of size $17 \times 17 \times 17$ by accounting for the isotopic scattering effects [29,30] and third-order anharmonicity.

To evaluate the effect of compositional disorder on the conductivity of $La_{1-x}Gd_xPO_4$, we employ the following computational protocol.

(1) We build a perfect $6 \times 6 \times 6$ supercell of the primitive cell of $LaPO_4$.

(2) We construct second-order force constants (fc2) for the perfect supercell. We do this by mapping the primitive-cell force constants into the supercell using the tool of Ref. [129].

(3) We use the pristine supercell fc2 computed at the previous point as a starting point to describe compositional disorder at eight different compositions $x \in [0.05, 0.15, 0.30, 0.50, 0.70, 0.85, 0.95, 1.00]$. Specifically, we use the mass-substitution approximation explained in Sec. III D 1 [see Eqs. (6) and (7)]. For each composition x, we scan the supercell sites containing La, and with probability x, we replace the mass of La atoms

with the mass of Gd [representative configurations are shown in Fig. 16(a)].

(4) We assess the dynamical stability of each of the eight compositionally disordered configurations by diagonalizing the mass-substituted, disordered dynamical matrix (6), and verifying that the vibrational density of states is nonzero only for positive values of the vibrational energy [Figs. 16(b) and 16(c)].

(5) We compute the velocity operator [Eq. (10)] for each disordered composition on the computationally converged $3 \times 3 \times 3$ **q** mesh (see Fig. 12 for convergence tests). In this step, to reduce the computational cost, we neglect the effect of the nonanalytical term correction [116]. We validate this approximation in Fig. 17 by showing its negligible effect on the thermal conductivity.

(6) We employ the velocity operator and the coarse-grained linewidth [Eq. (11)] to evaluate the Wigner thermal conductivity (1).

We note, in passing, that we considered one disordered configuration for each composition, since the convergence tests in Fig. 6 show that the total conductivities of different disordered cells of $La_{0.5}Gd_{0.5}PO_4$ larger than 1536 atoms
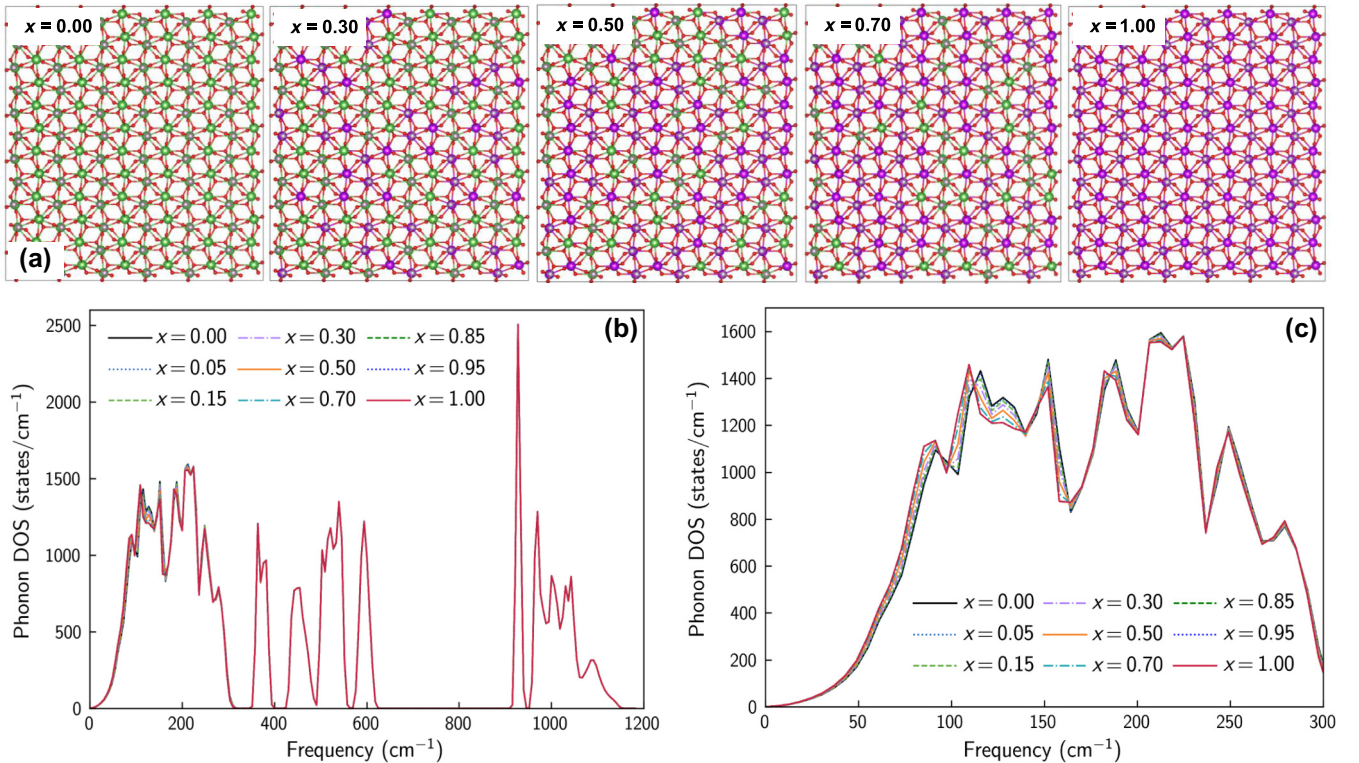

FIG. 16. Explicit simulation of harmonic vibrational properties of $La_{1-x}Gd_xPO_4$ alloys. (a) Front view of the 5184-atom disordered cell of $La_{1-x}Gd_xPO_4$ of different compositions x. The green, violet, red, and purple colors represent La, P, O, and Gd atoms, respectively. (b) Phonon density of states (DOS) as a function of x; for all the disordered configurations considered, the vibrational frequencies are real and positive, indicating dynamic stability. (c) Enlarged view of the phonon DOS in the range 50 to 300 cm^{-1}, where compositional disorder has the largest effects.
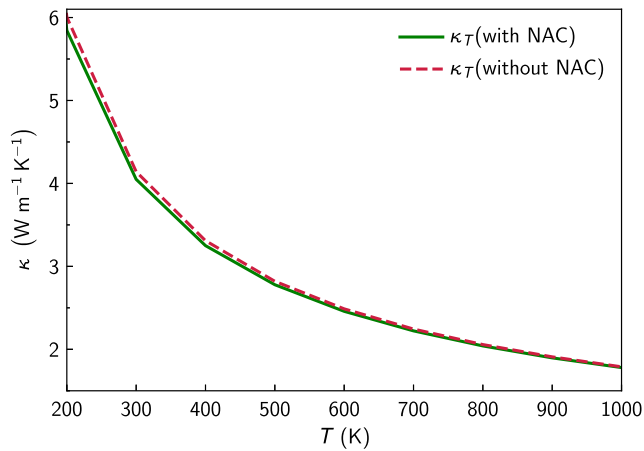
FIG. 17. Negligible effect of the nonanalytical term correction on the conductivity of pristine $LaPO_4$, computed using a perfect 5184-atom supercell (a $6 \times 6 \times 6$ repetition of the primitive cell) on a $3 \times 3 \times 3$ **q** mesh.

of the same composition $x = 0.5$ are practically indistinguishable.

[1] N. P. Padture, Advanced structural ceramics in aerospace propulsion, Nat. Mater. **15**, 804 (2016).

[2] D. R. Clarke, M. Oechsner, and N. P. Padture, Thermal-barrier coatings for more efficient gas-turbine engines, MRS Bull. **37**, 891 (2012).

[3] X. Zhang, Z. Deng, H. Li, J. Mao, C. Deng, C. Deng, S. Niu, W. Chen, J. Song, J. Fan, M. Liu, and K. Zhou, Al_2O_3-modified PS-PVD 7YSZ thermal barrier coatings for advanced gas-turbine engines, npj Mater. Degrad. **4**, 1 (2020).

[4] D. Tejero-Martin, C. Bennett, and T. Hussain, A review on environmental barrier coatings: History, current state of the art and future developments, J. Eur. Ceram. Soc. **41**, 1747 (2021).

[5] K. Leng, A. Rincon Romero, F. Venturi, I. Ahmed, and T. Hussain, Solution precursor thermal spraying of gadolinium zirconate for thermal barrier coating, J. Eur. Ceram. Soc. **42**, 1594 (2022).

[6] R. A. Miller, Thermal barrier coatings for aircraft engines: History and directions, J. Therm. Spray Technol. **6**, 35 (1997).

[7] B. Liu, Y. Liu, C. Zhu, H. Xiang, H. Chen, L. Sun, Y. Gao, and Y. Zhou, Advances on strategies for searching for next generation thermal barrier coating materials, J. Mater. Sci. Technol. **35**, 833 (2019).

[8] L. Xu, S. Bo, Y. Hongde, and W. Lei, Evolution of Rolls-Royce air-cooled turbine blades and feature analysis, Procedia Eng. **99**, 1482 (2015).

[9] C. Wan, W. Zhang, Y. Wang, Z. Qu, A. Du, R. Wu, and W. Pan, Glass-like thermal conductivity in ytterbium-doped lanthanum zirconate pyrochlore, Acta Mater. **58**, 6166 (2010).

[10] Y. Wang, F. Yang, and P. Xiao, Role and determining factor of substitutional defects on thermal conductivity:

A study of $La_2(Zr_{1-x}B_x)_2O_7$ (B = Hf, Ce, $0 \le x \le 0.5$) pyrochlore solid solutions, Acta Mater. **68**, 106 (2014).

[11] E. Martin, G. Ori, T.-Q. Duong, M. Boero, and C. Massobrio, Thermal conductivity of amorphous SiO_2 by first-principles molecular dynamics, J. Non-Cryst. Solids **581**, 121434 (2022).

[12] A. Bouzid, H. Zaoui, P. L. Palla, G. Ori, M. Boero, C. Massobrio, F. Cleri, and E. Lampin, Thermal conductivity of glassy $GeTe_4$ by first-principles molecular dynamics, Phys. Chem. Chem. Phys. **19**, 9729 (2017).

[13] T.-Q. Duong, C. Massobrio, G. Ori, M. Boero, and E. Martin, Thermal conductivity and transport modes in glassy $GeTe_4$ by first-principles molecular dynamics, Phys. Rev. Mater. **3**, 105401 (2019).

[14] A. Marcolongo, P. Umari, and S. Baroni, Microscopic theory and quantum simulation of atomic heat transport, Nat. Phys. **12**, 80 (2016).

[15] C. Carbogno, R. Ramprasad, and M. Scheffler, Ab initio Green-Kubo approach for the thermal conductivity of solids, Phys. Rev. Lett. **118**, 175901 (2017).

[16] M. Puligheddu, F. Gygi, and G. Galli, First-principles simulations of heat transport, Phys. Rev. Mater **1**, 060802 (2017).

[17] D. A. Broido, M. Malorny, G. Birner, N. Mingo, and D. A. Stewart, Intrinsic lattice thermal conductivity of semiconductors from first principles, Appl. Phys. Lett. **91**, 231922 (2007).

[18] G. Fugallo, M. Lazzeri, L. Paulatto, and F. Mauri, Ab initio variational approach for evaluating lattice thermal conductivity, Phys. Rev. B **88**, 045430 (2013).

[19] L. Paulatto, I. Errea, M. Calandra, and F. Mauri, First-principles calculations of phonon frequencies, lifetimes, and spectral functions from weak to strong anharmonicity: The example of palladium hydrides, Phys. Rev. B **91**, 054304 (2015).

[20] A. Cepellotti, J. Coulter, A. Johansson, N. S. Fedorova, and B. Kozinsky, Phoebe: A high-performance framework for solving phonon and electron Boltzmann transport equations, J. Phys. Mater. **5**, 035003 (2022).

[21] A. Togo, First-principles phonon calculations with Phonopy and Phono3py, J. Phys. Soc. Jpn. **92**, 012001 (2023).

[22] L. Chaput, Direct solution to the linearized phonon Boltzmann equation, Phys. Rev. Lett. **110**, 265506 (2013).

[23] T. Tadano, Y. Gohda, and S. Tsuneyuki, Anharmonic force constants extracted from first-principles molecular dynamics: Applications to heat transfer simulations, J. Phys.: Condens. Matter **26**, 225402 (2014).

[24] J. Carrete, B. Vermeersch, A. Katre, A. van Roekeghem, T. Wang, G. K. Madsen, and N. Mingo, almaBTE: A solver of the space–time dependent Boltzmann transport equation for phonons in structured materials, Comput. Phys. Commun. **220**, 351 (2017).

[25] L. Lindsay, A. Katre, A. Cepellotti, and N. Mingo, Perspective on *ab initio* phonon thermal transport, J. Appl. Phys. **126**, 050902 (2019).

[26] F. Knoop, M. Scheffler, and C. Carbogno, Ab initio Green-Kubo simulations of heat transport in solids: Method and implementation, Phys. Rev. B **107**, 224304 (2023).

[27] F. Knoop, T. A. Purcell, M. Scheffler, and C. Carbogno, Anharmonicity in thermal insulators: An analysis from first principles, Phys. Rev. Lett. **130**, 236301 (2023).

[28] M. Simoncelli, N. Marzari, and F. Mauri, Unified theory of thermal transport in crystals and glasses, Nat. Phys. **15**, 809 (2019).

[29] S.-i. Tamura, Isotope scattering of dispersive phonons in Ge, Phys. Rev. B **27**, 858 (1983).

[30] J. Garg, N. Bonini, B. Kozinsky, and N. Marzari, Role of disorder and anharmonicity in the thermal conductivity of silicon-germanium alloys: A first-principles study, Phys. Rev. Lett. **106**, 045901 (2011).

[31] S. Thébaud, C. A. Polanco, L. Lindsay, and T. Berlijn, Success and breakdown of the T-matrix approximation for phonon-disorder scattering, Phys. Rev. B **102**, 094206 (2020).

[32] S. Thébaud, T. Berlijn, and L. Lindsay, Perturbation theory and thermal transport in mass-disordered alloys: Insights from Green's function methods, Phys. Rev. B **105**, 134202 (2022).

[33] M. Simoncelli, N. Marzari, and F. Mauri, Wigner formulation of thermal transport in solids, Phys. Rev. X **12**, 041011 (2022).

[34] Y. Luo, X. Yang, T. Feng, J. Wang, and X. Ruan, Vibrational hierarchy leads to dual-phonon transport in low thermal conductivity crystals, Nat. Commun. **11**, 2554 (2020).

[35] P. B. Allen and J. L. Feldman, Thermal conductivity of glasses: Theory and application to amorphous Si, Phys. Rev. Lett. **62**, 645 (1989).

[36] E. Di Lucente, M. Simoncelli, and N. Marzari, Crossover from Boltzmann to Wigner thermal transport in thermoelectric skutterudites, Phys. Rev. Res. **5**, 033125 (2023).

[37] Y. Xia, V. Ozoliņš, and C. Wolverton, Microscopic mechanisms of glasslike lattice thermal transport in cubic $Cu_{12}Sb_4S_{13}$ tetrahedrites, Phys. Rev. Lett. **125**, 085901 (2020).

[38] A. Jain, Multichannel thermal transport in crystalline Tl_3VSe_4, Phys. Rev. B **102**, 201201 (2020).

[39] K. Pal, Y. Xia, and C. Wolverton, Microscopic mechanism of unusual lattice thermal transport in $TlInTe_2$, npj Comput. Mater. **7**, 5 (2021).

[40] G. Caldarelli, M. Simoncelli, N. Marzari, F. Mauri, and L. Benfatto, Many-body Green's function approach to lattice thermal transport, Phys. Rev. B **106**, 024312 (2022).

[41] L. Isaeva, G. Barbalinardo, D. Donadio, and S. Baroni, Modeling heat transport in crystals and glasses from a unified lattice-dynamical approach, Nat. Commun. **10**, 3853 (2019).

[42] N. W. Lundgren, G. Barbalinardo, and D. Donadio, Mode localization and suppressed heat transport in amorphous alloys, Phys. Rev. B **103**, 024204 (2021).

[43] Y. Liu, H. Liang, L. Yang, G. Yang, H. Yang, S. Song, Z. Mei, G. Csányi, and B. Cao, Unraveling thermal transport correlated with atomistic structures in amorphous gallium oxide via machine learning combined with experiments, Adv. Mater. **35**, 2210873 (2023).

[44] M. Simoncelli, F. Mauri, and N. Marzari, Thermal conductivity of glasses: First-principles theory and applications, npj Comput. Mater. **9**, 1 (2023).

[45] A. F. Harper, K. Iwanowski, W. C. Witt, M. C. Payne, and M. Simoncelli, Vibrational and thermal properties of amorphous alumina from first principles, Phys. Rev. Mater. **8**, 043601 (2024).

[46] A. Du, C. Wan, Z. Qu, and W. Pan, Thermal conductivity of monazite-type $REPO_4$ (RE = La, Ce, Nd, Sm, Eu, Gd), J. Am. Ceram. Soc. **92**, 2687 (2009).

[47] H. Dong, X. Chen, J. Li, P. Jia, Y. Shuang, Q. Sun, and W. Ma, Preparation and thermal properties of $LaPO_4$ ceramics, IOP Conf. Ser. Mater. Sci. Eng. **678**, 012079 (2019).

[48] C. Zhang, J. Fei, L. Guo, J. Yu, B. Zhang, Z. Yan, and F. Ye, Thermal cycling and hot corrosion behavior of a novel $LaPO_4$/YSZ double-ceramic-layer thermal barrier coating, Ceram. Int. **44**, 8818 (2018).

[49] K. Shijina, S. Sankar, M. Midhun, M. Firozkhan, B. N. Nair, K. G. Warrier, and U. N. S. Hareesh, Very low thermal conductivity in lanthanum phosphate–zirconia ceramic nanocomposites processed using a precipitation–peptization synthetic approach, New J. Chem. **40**, 5333 (2016).

[50] Y. Hikichi and T. Nomura, Melting temperatures of monazite and xenotime, J. Am. Ceram. Soc. **70**, C-252 (1987).

[51] M. R. Rafiuddin and A. P. Grosvenor, An investigation of the chemical durability of hydrous and anhydrous rare-earth phosphates, J. Nucl. Mater. **509**, 631 (2018).

[52] N. Clavier, R. Podor, and N. Dacheux, Crystal chemistry of the monazite structure, J. Eur. Ceram. Soc. **31**, 941 (2011).

[53] W. Min, D. Miyahara, K. Yokoi, T. Yamaguchi, K. Daimon, Y. Hikichi, T. Matsubara, and T. Ota, Thermal and mechanical properties of sintered $LaPO_4$-Al_2O_3 composites, Mater. Res. Bull. **36**, 939 (2001).

[54] J. C. Maxwell, *A Treatise on Electricity and Magnetism* (Oxford, Clarendon Press, 1873). http://archive.org/details/electricandmagne01maxwrich.

[55] I. Sevostianov, S. Mogilevskaya, and V. Kushch, Maxwell's methodology of estimating effective properties: Alive and well, Int. J. Eng. Sci. **140**, 35 (2019).

[56] M. Simoncelli, N. Marzari, and A. Cepellotti, Generalization of Fourier's law into viscous heat equations, Phys. Rev. X **10**, 011019 (2020).

[57] J. Dragašević and M. Simoncelli, Viscous heat backflow and temperature resonances in extreme thermal conductors, arXiv preprint, arXiv:2303.12777.

[58] L. Lindsay, First principles Peierls-Boltzmann phonon thermal transport: A topical review, Nanoscale Microscale Thermophys. Eng. **20**, 67 (2016).

[59] L. Paulatto, F. Mauri, and M. Lazzeri, Anharmonic properties from a generalized third-order *ab initio* approach: Theory and applications to graphite and graphene, Phys. Rev. B **87**, 214303 (2013).

[60] G. Fugallo, A. Cepellotti, L. Paulatto, M. Lazzeri, N. Marzari, and F. Mauri, Thermal conductivity of graphene and graphite: Collective excitations and mean free paths, Nano Lett. **14**, 6109 (2014).

[61] H. Casimir, Note on the conduction of heat in crystals, Physica **5**, 495 (1938).

[62] J. B. Krieger and G. J. Iafrate, Quantum transport for Bloch electrons in a spatially homogeneous electric field, Phys. Rev. B **35**, 9644 (1987).

[63] M. Simoncelli, D. Fournier, M. Marangolo, E. Balan, K. Béneut, B. Baptiste, B. Doisneau, N. Marzari, and F. Mauri, Temperature-invariant heat conductivity from compensating crystalline and glassy transport: From the Steinbach meteorite to furnace bricks, arXiv preprint, arXiv:2405.13161.

[64] A. Fiorentino, P. Pegolo, and S. Baroni, Hydrodynamic finite-size scaling of the thermal conductivity in glasses, npj Comput. Mater. **9,** 1 (2023).

[65] S. Baroni, S. de Gironcoli, A. Dal Corso, and P. Giannozzi, Phonons and related crystal properties from density-functional perturbation theory, Rev. Mod. Phys. **73,** 515 (2001).

[66] S. Lucas, E. Champion, D. Bernache-Assollant, and G. Leroy, Rare earth phosphate powders $RePO_4 \cdot nH_2O$ (Re = La, Ce or Y) II. Thermal behavior, J. Solid State Chem. **177,** 1312 (2004).

[67] A. Hirsch, P. Kegler, I. Alencar, J. Ruiz-Fuertes, A. Shelyug, L. Peters, C. Schreinemachers, A. Neumann, S. Neumeier, H.-P. Liermann, A. Navrotsky, and G. Roth, Structural, vibrational, and thermochemical properties of the monazite-type solid solution $La_{1-x}Pr_xPO_4$, J. Solid State Chem. **245,** 82 (2017).

[68] R. Cuscó, B. Gil, G. Cassabois, and L. Artús, Temperature dependence of Raman-active phonons and anharmonic interactions in layered hexagonal BN, Phys. Rev. B **94,** 155435 (2016).

[69] S. A. Prosandeev, U. Waghmare, I. Levin, and J. Maslar, First-order Raman spectra of $AB'_{1/2}B''_{1/2}O_3$ double per-ovskites, Phys. Rev. B **71,** 214307 (2005).

[70] D. Tuschel, Spectral resolution and dispersion in Raman spectroscopy, Spectroscopy **35,** 9 (2020).https://www.spectroscopyonline.com/view/spectral-resolution-and-dispersion-in-raman-spectroscopy

[71] M. Lazzeri and F. Mauri, First-principles calculation of vibrational Raman spectra in large systems: Signature of small rings in crystalline SiO_2, Phys. Rev. Lett. **90,** 036401 (2003).

[72] M. Bagheri and H.-P. Komsa, High-throughput computation of Raman spectra from first principles, Sci. Data **10,** 80 (2023).

[73] Q. Liang, S. Dwaraknath, and K. A. Persson, High-throughput computation and evaluation of Raman spectra, Sci. Data **6,** 135 (2019).

[74] J. M. Ziman, *Electrons and Phonons: The Theory of Transport Phenomena in Solids*, Oxford classic texts in the physical sciences (Clarendon Press ; Oxford University Press, Oxford, New York, 2001).

[75] T. Sun and P. B. Allen, Lattice thermal conductivity: Computations and theory of the high-temperature breakdown of the phonon-gas model, Phys. Rev. B **82,** 224305 (2010).

[76] W. Li and N. Mingo, Ultralow lattice thermal conductivity of the fully filled skutterudite $YbFe_4Sb_{12}$ due to the flat avoided-crossing filler modes, Phys. Rev. B **91,** 144304 (2015).

[77] P.-F. Lory, *et al.*, Direct measurement of individual phonon lifetimes in the clathrate compound $Ba_{7.81}Ge_{40.67}Au_{5.33}$, Nat. Commun. **8,** 491 (2017).

[78] Figure 15 shows that in $LaPO_4$ the phonon modes approximatively have linear dispersion relation up to about $\hbar\omega_D \simeq 100$ cm^{-1}. These modes give the largest

[79] K. Schulgasser, Bounds on the conductivity of statistically isotropic polycrystals, J. Phys. C: Solid State Phys. **10,** 407 (1977).

[80] A. Du, C. Wan, Z. Qu, R. Wu, and W. Pan, Effects of texture on the thermal conductivity of the $LaPO_4$ monazite, J. Am. Ceram. Soc. **93,** 2822 (2010).

[81] D. Zhang, Z. Zhao, B. Wang, S. Li, and J. Zhang, Investigation of a new type of composite ceramics for thermal barrier coatings, Mater. Des. **112,** 27 (2016).

[82] M. Li, Y. Cheng, L. Guo, Y. Zhang, C. Zhang, S. He, W. Sun, and F. Ye, Preparation of nanostructured $Gd_2Zr_2O_7$-$LaPO_4$ thermal barrier coatings and their calcium-magnesium-alumina-silicate (CMAS) resistance, J. Eur. Ceram. Soc. **37,** 3425 (2017).

[83] L. Guo, M. Li, S. He, C. Zhang, Q. Wang, and F. Ye, Preparation and hot corrosion behavior of plasma sprayed nanostructured $Gd_2Zr_2O_7$-$LaPO_4$ thermal barrier coatings, J. Alloys Compd. **698,** 13 (2017).

[84] L. Landau, E. Lifshitz, and L. Pitaevskij, *Statistical Physics, Part 2: Theory of the Condensed State* (Elsevier Science, Oxford, 1980), Vol. 9, https://books.google.co.in/books?id=NaB7oAkon9MC.

[85] S. Neumeier, P. Kegler, Y. Arinicheva, A. Shelyug, P. M. Kowalski, C. Schreinemachers, A. Navrotsky, and D. Bosbach, Thermochemistry of $La_{1-x}Ln_xPO_4$-monazites (Ln = Gd, Eu), J. Chem. Thermodyn. **105,** 396 (2017).

[86] J. Garg, *Thermal conductivity from first-principles in bulk, disordered, and nanostructured materials*, Thesis, Massachusetts Institute of Technology, See in particular Fig. 4.7 at page 77, https://dspace.mit.edu/handle/1721.1/65280.

[87] J. L. Braun, C. M. Rost, M. Lim, A. Giri, D. H. Olson, G. N. Kotsonis, G. Stan, D. W. Brenner, J.-P. Maria, and P. E. Hopkins, Charge-induced disorder controls the thermal conductivity of entropy-stabilized oxides, Adv. Mater. **30,** 1805004 (2018).

[88] D. G. Cahill, P. V. Braun, G. Chen, D. R. Clarke, S. Fan, K. E. Goodson, P. Keblinski, W. P. King, G. D. Mahan, A. Majumdar, H. J. Maris, S. R. Phillpot, E. Pop, and L. Shi, Nanoscale thermal transport. II. 2003–2012, Appl. Phys. Rev. **1,** 011305 (2014).

[89] H. R. Seyf, L. Yates, T. L. Bougher, S. Graham, B. A. Cola, T. Detchprohm, M.-H. Ji, J. Kim, R. Dupuis, W. Lv, and A. Henry, Rethinking phonons: The issue of disorder, npj Comput. Mater. **3,** 49 (2017).

[90] M. B. Maccioni, R. Farris, and V. Fiorentini, Ab initio thermal conductivity of thermoelectric Mg_3Sb_2: Evidence for dominant extrinsic effects, Phys. Rev. B **98,** 220301 (2018).

[91] T. Pandey, D. S. Parker, and L. Lindsay, Ab initio phonon thermal transport in monolayer InSe, GaSe, GaS, and alloys, Nanotechnology **28,** 455706 (2017).

[92] S. N. Khatami and Z. Ăksamija, Lattice thermal conductivity of the binary and ternary group-IV alloys Si-Sn, Ge-Sn, and Si-Ge-Sn, Phys. Rev. Appl. **6,** 014015 (2016).

[93] M. R. Winter and D. R. Clarke, Oxide materials with low thermal conductivity, J. Am. Ceram. Soc. **90,** 533 (2007).

[94] N. A. Katcho, N. Mingo, and D. A. Broido, Lattice thermal conductivity of $(Bi_{1-x}Sb_x)_2Te_3$ alloys with

contribution to κ_P, and their Debye temperature is approximatively $T_D = \hbar\omega_D/k_B \approx 144$ K.

embedded nanoparticles, Phys. Rev. B **85,** 115208 (2012).

[95] P. B. Allen and J. L. Feldman, Thermal conductivity of disordered harmonic solids, Phys. Rev. B **48,** 12581 (1993).

[96] J. L. Feldman, M. D. Kluge, P. B. Allen, and F. Wooten, Thermal conductivity and localization in glasses: Numerical study of a model of amorphous silicon, Phys. Rev. B **48,** 12589 (1993).

[97] For example, for a 1536-atom model, a calculation on a $5 \times 5 \times 5$ **q** mesh corresponds to simulating a system that contains $1536 \cdot 5^3 = 192\,000$ atoms, but with disorder length scale limited to the size of the reference cell containing 1536 atoms.

[98] By the "**q**-sampling limit" we mean the regime in which increasing the **q** mesh yields negligible changes on the conductivity.

[99] The decrease of particlelike conductivity upon increasing disorder was already noted in Ref. [86] for $Si_{0.5}Ge_{0.5}$ alloys. This can be intuitively understood by recalling that disorder induces repulsion between vibrational eigenstates, lowering the phonon group velocities [130], and consequently lowering the particlelike thermal conductivity.

[100] W. Li, L. Lindsay, D. A. Broido, D. A. Stewart, and N. Mingo, Thermal conductivity of bulk and nanowire $Mg_2Si_xSn_{1-x}$ alloys from first principles, Phys. Rev. B **86,** 174307 (2012).

[101] C. Melis and L. Colombo, Lattice thermal conductivity of $Si_{1-x}Ge_x$ nanocomposites, Phys. Rev. Lett. **112,** 065901 (2014).

[102] M. Arrigoni, J. Carrete, N. Mingo, and G. K. H. Madsen, First-principles quantitative prediction of the lattice thermal conductivity in random semiconductor alloys: The role of force-constant disorder, Phys. Rev. B **98,** 115205 (2018).

[103] D. M. Rowe, *Thermoelectrics Handbook* (Taylor & Francis, New York, 2005).

[104] B. Abeles, Lattice thermal conductivity of disordered semiconductor alloys at high temperatures, Phys. Rev. **131,** 1906 (1963).

[105] C. L. Wan, W. Pan, Q. Xu, Y. X. Qin, J. D. Wang, Z. X. Qu, and M. H. Fang, Effect of point defects on the thermal transport properties of $(La_xGd_{1-x})_2Zr_2O_7$: Experiment and theoretical model, Phys. Rev. B **74,** 144109 (2006).

[106] H. Chen, Y. Gao, S. Tao, Y. Liu, and H. Luo, Thermophysical properties of lanthanum zirconate coating prepared by plasma spraying and the influence of post-annealing, J. Alloys Compd. **486,** 391 (2009).

[107] A. Pazhedath, L. Bastonero, N. Marzari, and M. Simoncelli, Supporting data for "First-principles characterization of thermal conductivity in LaPO4-based alloys", (2023), https://doi.org/10.24435/materialscloud:ft-j0.

[108] Y. Ni, J. M. Hughes, and A. N. Mariano, Crystal chemistry of the monazite and xenotime structures, Am. Mineral. **80,** 21 (1995).

[109] A. A. Maradudin and S. H. Vosko, Symmetry properties of the normal vibrations of a crystal, Rev. Mod. Phys. **40,** 1 (1968).

[110] S. G. Mayo, F. Yndurain, and J. M. Soler, Band unfolding made simple, J. Phys.: Condens. Matter **32,** 205902 (2020).

[111] P. Giannozzi, *et al.*, Advanced capabilities for materials modelling with quantum ESPRESSO, J. Phys.: Condens. Matter **29,** 465901 (2017).

[112] J. P. Perdew, A. Ruzsinszky, G. I. Csonka, O. A. Vydrov, G. E. Scuseria, L. A. Constantin, X. Zhou, and K. Burke, Restoring the density-gradient expansion for exchange in solids and surfaces, Phys. Rev. Lett. **100,** 136406 (2008).

[113] G. Prandini, A. Marrazzo, I. E. Castelli, N. Mounet, and N. Marzari, Precision and efficiency in solid-state pseudopotential calculations, npj Comput. Mater. **4,** 72 (2018).

[114] K. Lejaeghere, *et al.*, Reproducibility in density functional theory calculations of solids, Science **351,** aad3000 (2016).

[115] H. J. Monkhorst and J. D. Pack, Special points for Brillouin-zone integrations, Phys. Rev. B **13,** 5188 (1976).

[116] X. Gonze and C. Lee, Dynamical matrices, born effective charges, dielectric permittivity tensors, and interatomic force constants from density-functional perturbation theory, Phys. Rev. B **55,** 10355 (1997).

[117] W. Li, J. Carrete, N. A. Katcho, and N. Mingo, ShengBTE: A solver of the Boltzmann transport equation for phonons, Comput. Phys. Commun. **185,** 1747 (2014).

[118] A. Togo and I. Tanaka, First principles phonon calculations in materials science, Scr. Mater. **108,** 1 (2015).

[119] F. Eriksson, E. Fransson, and P. Erhart, The hiphive package for the extraction of high-order force constants by machine learning, Adv. Theory Simul. **2,** 1800184 (2019).

[120] A. Togo, L. Chaput, and I. Tanaka, Distributions of phonon lifetimes in Brillouin zones, Phys. Rev. B **91,** 094306 (2015).

[121] L. Bastonero and N. Marzari, Automated all-functionals infrared and Raman spectra, npj Comput. Mater. **10,** 55 (2024).

[122] P. Umari and A. Pasquarello, Density functional theory with finite electric field, Int. J. Quantum Chem. **101,** 666 (2005).

[123] S. Huber, *et al.*, AiiDA 1.0, a scalable computational infrastructure for automated reproducible workflows and data provenance, Sci. Data **7,** 300 (2020).

[124] M. Uhrin, S. P. Huber, J. Yu, N. Marzari, and G. Pizzi, Workflows in AiiDA: Engineering a high-throughput, event-based engine for robust and modular computational workflows, Comput. Mater. Sci. **187,** 110086 (2021).

[125] I. Souza, J. Íñiguez, and D. Vanderbilt, First-principles approach to insulators in finite electric fields, Phys. Rev. Lett. **89,** 117602 (2002).

[126] P. Umari and A. Pasquarello, Ab initio molecular dynamics in a finite homogeneous electric field, Phys. Rev. Lett. **89,** 157602 (2002).

[127] R. E. Peierls, *Quantum Theory of Solids*, Oxford Classics Series (Clarendon Press, Oxford, 2001).

[128] R. J. Hardy, Energy-flux operator for a lattice, Phys. Rev. **132,** 168 (1963).

[129] J. Berges, A. Schobert, van Loon, E. G. C. P., M. Rösner, and T. O. Wehling, elphmod: Python modules for electron-phonon models (2022), https://doi.org/10.5281/zenodo.5919991.

[130] M. V. Simkin and G. D. Mahan, Minimum thermal conductivity of superlattices, Phys. Rev. Lett. **84,** 927 (2000).